remote sensing

Article

Regulatory Effect Evaluation of Warming and Cooling Factors on Urban Land Surface Temperature Based on Multi-Source Satellite Data

Yuchen Wang [1], Yu Zhang [2,*] and Nan Ding [2]

1 Department of Big Data Management and Application, School of Management Science and Engineering, Xuzhou University of Technology, Xuzhou 221018, China; wangyuchen@cumt.edu.cn
2 Institute of Land Resource, School of Geography, Geomatics and Planning, Jiangsu Normal University, Xuzhou 221116, China; metdingnan@jsnu.edu.cn
* Correspondence: yuzhang@jsnu.edu.cn

Abstract: Various physical characteristics of urban impervious surfaces (ISAs) and urban green spaces (UGSs) collectively regulate environmental temperatures through heating and cooling processes. However, current research often analyzes each regulating factor as an independent variable when examining its relationship with land surface temperature (LST), with limited studies considering the combined contribution weights of all regulating factors. Based on multi-source remote sensing data and ground observations from the near summers of 2014, 2016, 2017, and 2018 in the built-up area of Xuzhou City, numerical values and spatial distributions of 15 regulating factors, including ISA density (f_i), land surface albedo (Albedo), population density (Population), anthropogenic heat flux (AHF), maximum ISA patch index (LPI_{ISA}), natural connectivity of ISA patches ($COHESION_{ISA}$), aggregation index of ISA patches (AI_{ISA}), average shape index of ISA patches ($SHAPE\_MN_{ISA}$), UGS density (f_v), evapotranspiration (ET), UGS shading index (UGSSI), maximum UGS patch index (LPI_{UGS}), natural connectivity of UGS patches ($COHESION_{UGS}$), aggregation index of UGS patches (AI_{UGS}), and average shape index of UGS patches ($SHAPE\_MN_{UGS}$), were separately extracted within the study area. Using geographically weighted regression models and bivariate spatial autocorrelation models, we separately obtained the quantitative and spatial correlations between the 15 regulating factors and LST. The results revealed that all selected regulating factors exhibited high goodness-of-fit and significant spatial correlations with LST, which led to their categorization into eight warming factors and seven cooling factors. The factor detection of the Geographic Detector further reveals the combined contribution of all regulating factors to LST. The results indicate that cooling factors collectively have higher explanatory power for LST compared to warming factors, with UGSSI contributing the most to LST, while Population contributed the least. Furthermore, the interaction detection results of the Geographic Detector have highlighted variations in the explanatory power of different factor combinations on LST. Ultimately, it has identified factor combinations that have proven to be most effective in mitigating the urban heat environment across three scenarios: warming factors alone, cooling factors alone, and a combination of both warming and cooling factors. The suggested factor combinations are as follows: $f_i \cap$ Albedo, $f_i \cap LPI_{ISA}$, UGSSI $\cap f_v$, UGSSI $\cap LPI_{UGS}$, $f_i \cap$ UGSSI, and Albedo $\cap$ UGSSI. Therefore, our findings hold the potential to provide a valuable reference for urban planning and climate governance. Tailoring factor combinations to the local context and selecting the most effective ones can enable cost-effective mitigation of the urban heat environment.

Keywords: urban thermal environment; impervious surface; green space; landscape pattern; Landsat 8

Citation: Wang, Y.; Zhang, Y.; Ding, N. Regulatory Effect Evaluation of Warming and Cooling Factors on Urban Land Surface Temperature Based on Multi-Source Satellite Data. *Remote Sens.* **2023**, *15*, 5025. https://doi.org/10.3390/rs15205025

Academic Editors: Yuji Murayama, Ahmed Derdouri and Ruci Wang

Received: 16 September 2023
Revised: 9 October 2023
Accepted: 17 October 2023
Published: 19 October 2023

1. Introduction

In the course of urbanization, natural land surfaces are substituted with impervious surface areas (ISA) such as buildings and roads, leading to alterations in the thermal conductivity, water retention, and land albedo [1–3]. Simultaneously, the significant reduction in vegetation cover within the region also diminishes the water and heat exchange processes involved in evapotranspiration (ET) [2]. The series of changes in land surfaces have exerted a considerable impact on regional climate and urban environments, with the most conspicuous feature being the urban heat island (UHI) effect. The urban heat island (UHI) effect describes a situation in which the atmospheric or land surface temperature (LST) in a city experiences a marked increase compared to those in the adjacent suburban regions [4]. The continuous environmental heating associated with UHI leads to increased energy consumption, carbon emissions, and air pollution [5–7]. Furthermore, This presents a significant danger to the well-being of city dwellers and the quality of their living environment [8,9]. Energy consumption in urban areas for mitigating high temperatures can increase by up to 120% [10], and residents face elevated risks of heatstroke, cardiovascular, and respiratory diseases due to heatwaves [11]. Therefore, it is crucial to investigate and grasp the regulatory effects and contributions of warming and cooling factors on urban LST.

The generation of the UHI effect is closely linked to shifts in land surface features, alongside population density and the heat emissions from human activities. The combined effects of population growth and urban expansion are considered to be responsible for creating extreme urban heat climates, as the increasing population density leads to higher consumption of regional electricity and water resources [12,13]. Research on cities in East Africa, including Addis, Ababa, and Nairobi, likewise indicates a strong supportive correlation between population and climate warming [14]. The anthropogenic heat generated by human industrial, transportation, and residential activities is also a significant heat source within urban areas [15]. In regions of North America and Eurasia with high latitudes, anthropogenic heat can lead to temperature increases of approximately 1 °C in winter and autumn [16]. In the central area of Tokyo, Japan, anthropogenic heat has been detected at levels as high as 1590 W/m^2, corresponding to temperature increases of up to 2.5 °C [17]. Furthermore, the impact of anthropogenic heat on wind turbulence intensity can indirectly affect the regulation of regional thermal environments [18].

Urban green spaces (UGSs) [19], comprising forests, artificial green landscapes, and vegetation belts, constitute a form of natural land surface retained within urban areas. The temperatures within UGSs are significantly lower than those of the surrounding ISAs, creating what is known as an urban cool island effect [20]. This phenomenon represents an important approach to mitigating the urban heat challenges and enhancing the quality of residents' lives. The capacity of UGSs to lower urban temperatures is primarily achieved through vegetation shading and ET [21]. Tree canopies reduce the incoming solar radiation on urban surfaces, thereby reducing the heat storage and convection at the land surface, which directly lowers the LST [22,23]. The remote sensing observations of Tampa and New York City conducted between 07:30 and 10:30 local time have demonstrated a significant negative correlation ($p < 0.01$) between the proportion of tree canopy coverage and LST. Moreover, it was found that a greater expanse of the tree canopy results in a stronger cooling effect [24]. ET primarily involves the absorption of heat from the surroundings through vegetation transpiration and soil moisture evaporation to reduce the environmental temperature [25]. It has been reported that each additional 10 W/m^2 of ET can lower the LST by 0.56 °C [26].

In addition to the factors mentioned above, when ISAs and UGSs are treated as two distinct land cover types, their spatial distribution and structure can also influence environmental temperatures [27]. Landscape factors such as the size, shape, aggregation, and natural connectivity of ISA and UGS patches have been shown in previous studies to be correlated with LST [28,29]. However, it is worth noting that this correlation tends to be more pronounced in high-density ISA or UGS patches.

The impact of various factors on urban land surface temperature (LST) has already been clearly revealed by previous research [28]. However, within these studies, there are still two issues that require further exploration and resolution. When investigating the relationship between various factors and the urban heat island (UHI) effect, the focus has often been on individual or a few factors, with little comprehensive consideration of the combined impact of various warming and cooling variables on the urban thermal environment within the same context [30]. Another pressing issue that needs to be addressed is that although some studies have simultaneously investigated multiple relevant indices of impervious surfaces and vegetation and their correlation with LST, all these factors are still separately analyzed. Furthermore, the results are often represented using univariate statistical correlation coefficients, linear fitting goodness, and spatial correlation coefficients [31,32], which fail to reflect the contribution of each factor to LST under the combined effects of multiple variables. This is primarily due to the difficulty of using a simple regression equation to model the complex mathematical relationships between all factors and the LST [28]. Therefore, in our study, we attempted to address these research gaps through several aspects: firstly, 15 factors representing different regulating characteristics were comprehensively selected based on previous research to analyze the combined impact of warming and cooling factors on LST within the same context. Next, these factor values were inferred based on multi-source satellite data and ground observations, and the quantity and spatial correlation relationships between each regulating factor and LST were analyzed and compared using graphic weighted regression (GWR) models and bivariate spatial autocorrelation models. Finally, factor detection and interaction detection were conducted using geographic detectors to reveal the contributions of each factor to LST under the combined influence of multiple factors, which can help in providing the optimal factor combinations for mitigating the urban heat environment under different scenarios. The technical route of this study is shown in Figure 1.

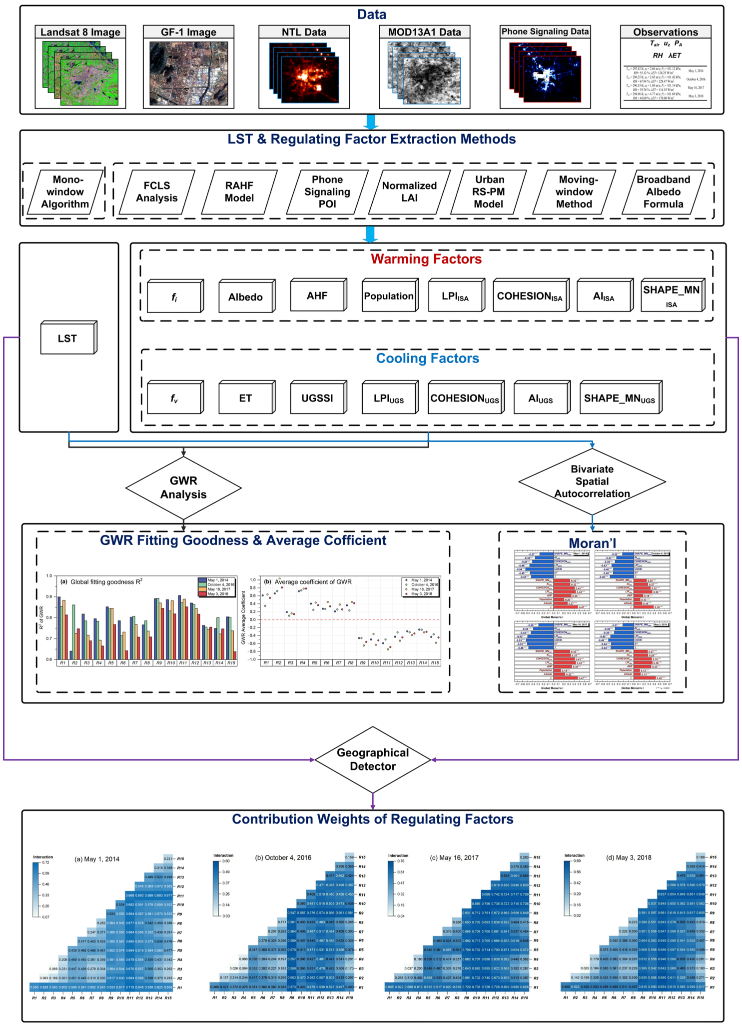

Figure 1. The technical route of this study.

2. Materials and Methods

2.1. Study Area

Xuzhou City is situated in the eastern part of China and is under the jurisdiction of Jiangsu Province. It experiences a mid-latitude monsoonal climate and exhibits distinct seasonal characteristics. Xuzhou's topography is primarily characterized by plains, constituting approximately 90% of the city's total area and having a mean elevation of around 40 m. Xuzhou is an important gateway city in eastern China. From 2006 to 2022, the urbanization rate in Xuzhou has risen from 44.8% to 66.2% (proportion of urban population in the total population of the administrative regions), with the urban population reaching 6.026 million people. Xuzhou not only boasts developed industrial, energy, and trade sectors but also plays a pivotal role in connecting transportation networks across eastern China. In the rapid urbanization process, Xuzhou has witnessed significant social and economic development. At the same time, it has also experienced notable changes in urban environment and climate, particularly the UHI effect resulting from land cover changes and energy consumption. In this study, based on the existing administrative boundaries of Xuzhou's Quanshan District, Gulou District, Jiuli District, and Yunlong District, we manually delineated the boundaries of a large number of aggregated construction land patches in the Landsat 8 image from 3 May 2018, and, finally, the extracted Xuzhou's built-up area and its adjacent suburban regions, where the UHI effect is most pronounced, has been selected as the research area (Figure 2).

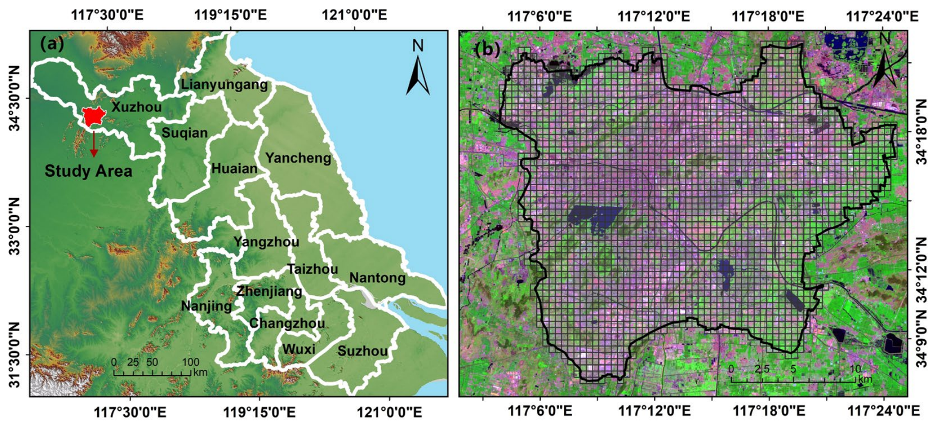

Figure 2. (**a**) Study area in Xuzhou, Jiangsu Province; (**b**) study area (Landsat 8 image from 3 May 2018; false color fusion of 7, 5, and 3 bands) with fishnet.

2.2. Data

Four sets of Landsat 8 images for local daytimes in 2014, 2016, 2017, and 2018 were downloaded from the United States Geological Survey (USGS) [33], and all Landsat 8 data were preprocessed through radiometric calibration, atmospheric correction (using the Fast Line-of-Sight Atmospheric Analysis of Spectral Hypercubes model, FLAASH), and geometric correction (with the GF-1 PAN band as the reference image). The multispectral bands 1–7 were used to extract information related to ISA and UGS fractions, as were relevant land surface parameters within the study area, while thermal infrared band 10 was employed for the inversion of LST. It is worth noting that Landsat 8 data was acquired in May for the years 2014, 2017, and 2018, while in 2016, it was acquired in October. This was primarily done to align with the flux observation data used later in the study. On 4 October 2016, the study area was in the late summer period, but the average temperature on that day was only about 1 °C different from the other three periods (early summer). Therefore, we can consider that the urban LST simulated for 2016 is unlikely to result in significant differences.

The monthly composites of the Suomi National Polar-orbiting Partnership (Suomi-NPP) visible infrared imaging radiometer suite (VIIRS) nighttime light (NTL) data downloaded from the Earth Observation Group (EOG) [34] and the Multi-temporal Terra moderate resolution imaging spectroradiometer (MODIS) NDVI products (MOD13A1) downloaded from the Level-1 and Atmosphere Archive & Distribution System Distributed Active Archive Center (LAADS DAAC) [35] were jointly used to estimate the Anthropogenic Heat Flux (AHF) in the study area. High-resolution remote sensing data from GF-1, acquired on 5 October 2016 and obtained from the China Centre for Resource Satellite Data and Application (CASC) [36], were used to validate the accuracy of ISA and UGS fractions extraction.

Additionally, ground observation data required for LST inversion and ET estimation and validation include air temperature (T_{air}), air relative humidity (RH), wind speed (u_z), atmospheric pressure (P_A), and latent heat flux (λET) were all obtained from the Collaborative Observation Test Site of China University of Mining and Technology (located at 117°8′27.98″E, 34°13′18.58″N in the study area). This site is equipped with a meteorological observation station and a flux tower equipped with eddy covariance (EC) instruments. Population density data for the study area were obtained from 100 m resolution mobile signaling data provided by China Mobile Communications. All of these data are presented in Table 1. In order to facilitate the comparison of results for the 15 regulating factors and LST, the spatial resolution of all outcomes will be resampled to 500×500 m^2 based on the pixel aggregate method to ensure consistency.

Table 1. Satellite data and ground observations.

Data Source	Spatial Resulation	Data	Acquisition Date
Landsat 8	OLI: 30 m TIRS: 100 m	LC81210362014121LGN00 (Cloud Cover: 0.88%)	1 May 2014 (Local Time: 10:42:29)
		LC81220362016278LGN00 (Cloud Cover: 1.23%)	4 October 2016 (Local Time: 10:49:11)
		LC81220362017136LGN00 (Cloud Cover: 0.41%)	16 May 2017 (Local Time: 10:48:22)
		LC81220362018123LGN00 (Cloud Cover: 0.14%)	3 May 2018 (Local Time: 10:48:04)
NPP VIIRS NTL	500 m	SVDNB_npp_20140501-20140531_75N060E_vcmcfg_v10_c201502061154	May 2014
		SVDNB_npp_20161001-20161031_75N060E_vcmcfg_v10_c201612011122	October 2016
		SVDNB_npp_20170501-20170531_75N060E_vcmcfg_v10_c201706021500	May 2017
		SVDNB_npp_20180501-20180531_75N060E_vcmcfg_v10_c201806061100	May 2018
MOD13A1	500 m	MOD13A1.A2014129.h27v05.006.2015281104645	9 May 2014
		MOD13A1.A2016273.h27v05.006.2016292070735	29 September 2016
		MOD13A1.A2017129.h27v05.006.2017145230514	9 May 2017
		MOD13A1.A2018129.h27v05.006.2018151110825	9 May 2018
GF-1	PAN: 2 m MSS: 8 m	GF2_PMS2_E117.2_N34.2_20161005_L1A0001867916	5 October 2016
Mobile Phone Signaling Data	100 m	Mobile Phone Signaling Data_Xuzhou_2014	2014
		Mobile Phone Signaling Data _Xuzhou_2016	2016
		Mobile Phone Signaling Data _Xuzhou_2017	2017
		Mobile Phone Signaling Data _Xuzhou_2018	2018
Meteorological and Flux Observations	/	T_{air} = 24.27 °C; u_z = 2.66 m/s; P_A = 101.12 kPa; RH= 55.12%; λET= 128.25 W/m^2	1 May 2014
		T_{air} = 23.10 °C; u_z = 2.65 m/s; P_A = 101.42 kPa; RH = 67.94%; λET = 228.47 W/m^2	4 October 2016
		T_{air} = 23.18 °C; u_z = 1.69 m/s; P_A = 101.19 kPa; RH = 39.76%; λET = 114.19 W/m^2	16 May 2017
		T_{air} = 21.81 °C; u_z = 4.77 m/s; P_A = 101.69 kPa; RH = 48.00%; λET = 178.00 W/m^2	3 May 2018

2.3. LST Inversion

For Landsat 8 TIRS Band 10, the recommended single-channel algorithm by USGS can be applied for LST retrieval [37,38]. In addition to the multispectral and thermal infrared bands of remote sensing imagery, the improved mono-window algorithm [39] only requires two atmospheric parameters: T_{air} and atmospheric transmittance (τ). As a result, it is widely utilized for calculating surface temperatures from Landsat 8 data. The calculation equations are as follows:

$$LST = \{a(1 - C - D) + [b(1 - C - D) + C + D]T_{10} - DT_{air\_e}\}/C \quad (1)$$

$$C = \varepsilon\tau \quad (2)$$

$$D = (1 - \tau)[1 + (1 - \varepsilon)\tau] \quad (3)$$

where a = −62.7182 and b = 0.4339 are the coefficients of the Planck blackbody radiation equation for the thermal infrared band (0~70 °C); T_{10} is the brightness temperature observed directly by the satellite; T_{air_e} is the effective atmospheric temperature, which can be calculated using an empirical formula based on near-surface air temperature [40]; ε represents the surface emissivity, which can be calculated separately for natural surface and ISAs based on the fractional vegetation coverage index (P_v); and τ can be calculated based on its linear relationship with the atmospheric water content during mid-latitude summer [39,41].

$$T_{10} = K_2/ln(1 + K_1/L_{10}) \quad (4)$$

$$T_{air\_e} = 16.0110 + 0.9262T_{air} \quad (5)$$

$$\varepsilon_{veg} = P_v R_v \varepsilon_v + (1 - P_v)R_s\varepsilon_s + d_\varepsilon \quad (6)$$

$$\varepsilon_{ISA} = P_v R_v \varepsilon_v + (1 - P_v)R_i\varepsilon_i + d_\varepsilon \quad (7)$$

where K_1 and K_2 are predefined constants for the Landsat 8 satellite, which can be obtained from the header file; L_{10} is the radiance calculated from the thermal infrared band; R_v, R_s, and R_i are the temperature ratios for vegetation, soil, and ISAs, which can be calculated using empirical formulas; and ε_v, ε_s, and ε_i are the emissivity constants for pure vegetation, soil, and ISA pixels, respectively.

2.4. Regulating Factors Selection and Extraction

2.4.1. Regulating Factors Selection

Based on previous studies that have demonstrated various factors that can significantly affect LST, we selected eight representative warming factors and seven cooling factors from five aspects, land cover density, land surface spectral characteristics, human activities, vegetation physical properties, and spatial pattern of land patches, in order to analyze the comprehensive regulatory effects of these 15 variables on urban LST under the same context. All factors are shown in Table 2.

2.4.2. ISA and UGS Components Extraction

In urban Landsat 8 imagery, individual pixels often contain a fusion of ISAs, vegetation, and soil endmembers. Traditional land cover classification methods are unable to identify subpixel fraction information. Therefore, the fully constrained linear spectral mixture analysis (FCLS) [55] is used to extract the fractions of ISA and UGS components within mixed pixels in the study area. Compared to the conventional linear spectral mixture analysis [56], the FCLS not only imposes non-negativity constraints but also enforces that the sum of all component fractions within each pixel equals 1. This additional constraint ensures more accurate decomposition results. Based on field surveys in the Xuzhou region, the endmembers of mixed pixels can be categorized into woodland, grassland, soil, and high- and low-albedo ISAs. It is worth noting that water bodies in urban areas typically exist as separate patches, so masking out water bodies from the imagery before performing the mixed pixel decomposition can help improve accuracy. Based on the results of the mixed pixel decomposition, the abundance of woodland and grassland endmembers are summed to create the UGS density (f_v), while the abundance of high- and low-albedo ISA endmembers are summed to create the ISA density (f_i).

$$\overline{R_b} = \frac{R_b}{\frac{1}{N}\sum_{b=1}^{N} \times R_b} \times 100 \tag{8}$$

$$\overline{R_b} = \sum_{x=1}^{N} f_x \overline{R_{x,b}} + e_b \tag{9}$$

$$\sum_{x=1}^{N} f_x = 1, \ \ f_x \geq 0 \tag{10}$$

where $\overline{R_b}$, R_b, and $\overline{R_{x,b}}$ represent the normalized reflectance, initial reflectance, and the reflectance of endmember x, respectively, for a pixel.

Table 2. Source and explanation of the 15 regulating factors.

Factor	Correction Type with LST	Reference	Explaination
f_i	Positive	[42]	Area porportion (density) of ISAs in a mixture pixel
Albedo	Positive	[43]	Land surface albedo
Population	Positive	[44,45]	Population density within an area
AHF	Positive	[17,46]	Anthropogenic heat flux
LPI_{ISA}	Positive	[47]	Porportion of the largest patch with high ISA density
$COHESION_{ISA}$	Positive	[29]	Natural connectivity degree between patches with high ISA density
AI_{ISA}	Positive	[48]	Aggregation degree of patches with high ISA density
$SHAPE\_MN_{ISA}$	Positive	[29]	Mean shape index of patches with high ISA density
f_v	Negative	[20]	Area porportion (density) of UGSs in a mixture pixel
ET	Negative	[28,49,50]	Evaportranspiration
UGSSI	Negative	[24,51]	Shading index of UGSs
LPI_{UGS}	Negative	[52]	Porportion of the largest patch with high UGS density
$COHESION_{UGS}$	Negative	[28]	Natural connectivity degree between patches with high UGS density
AI_{UGS}	Negative	[53]	Aggregation degree of patches with high UGS density
$SHAPE\_MN_{UGS}$	Negative	[54]	Mean shape index of patches with high UGS density

2.4.3. AHF Estimation

NTL data can capture faint near-infrared radiation from the Earth's surface during nighttime, including the lights from urban areas, even in smaller residential settlements, as well as traffic and other persistent light sources. It serves as a suitable spatial substitute for socioeconomic and energy consumption statistics [57]. A significant correlation between NTL brightness and AHF has been demonstrated, allowing for the spatial estimation of AHF using this relationship [58,59]. Combining NTL data with vegetation indices can mitigate the oversaturation issue in NTL data to some extent, effectively enhancing the differentiation and discriminative ability of urban NTL brightness, thereby improving the fit between NTL and AHF [60,61]. Therefore, based on NPP/VIIRS and MOD13A1 data, a refined AHF (RAHF) model [62] was developed to estimate gridded AHF, which exhibits a higher goodness of fit (R^2 = 0.989). The equations are as follows:

$$AHF = 48.287HSI^2 - 17.716HSI + 2.541 \quad (11)$$

$$HSI = \frac{(1 - NDVI_{max}) + NTL_{nor}}{(1 - NTL_{nor}) + NDVI_{max} + NTL_{nor} \times NDVI_{max}} \quad (12)$$

where HSI represents the human settlement index; $NDVI_{max}$ is the maximum value of the normalized difference vegetation index ($NDVI$) within the study area, which was calculated from MOD13 products; and NTL_{nor} represents the normalized NTL data.

2.4.4. Spatial Simulation of Resident Population

Obtaining high-resolution spatial distribution of urban populations has always been a challenging task. Traditional population data relies heavily on population censuses, but this approach has long update cycles and provides population distribution characteristics only at the administrative level, making it suitable for large regional and national-scale studies but not for urban areas. Point of Interest (POI) data obtained from various sources has now become a crucial basis for spatial analysis of geographic features [63]. With the widespread use of smartphones in today's society, the spatial location information of smartphone users can be marked and generate POI data through signaling interactions between mobile phones and networks. These data can generate the most accurate representation of the regional population spatial distribution [64]. We utilized spatial location data from China Mobile Communications for the years 2014, 2016, 2017, and 2018 to simulate the geographical location of Xuzhou's permanent population for each period.

2.4.5. Land Surface Albedo Calculation

For Landsat TM/ETM data, Liang et al. [65] recommended using five bands, including blue (b_{Blue}, 0.45–0.52 μm), red (b_{Red}, 0.63–0.69 μm), near-infrared (b_{NIR}, 0.77–0.90 μm), short wavelength infra-red 1 (b_{SWIR1}, 1.55–1.75 μm), and short wavelength infra-red 2 (b_{SWIR2}, 2.09–2.35 μm) to calculate land surface albedo. Since Landsat 8 data has corresponding bands with very similar bandwidths to Landsat TM/ETM data and shares the same spatial resolution, Liang et al.'s method is also applicable to the Landsat 8 data [66].

$$\begin{gathered} Albedo = 0.356b_{blue} + 0.130b_{red} + 0.373b_{NIR} + 0.085b_{SWIR1} + 0.072b_{SWIR2} \\ -0.0018 \end{gathered} \quad (13)$$

2.4.6. Landscape Pattern Calculation

The landscape patterns of ISA and UGS patches, including LPI, COHESION, AI, and SHAPE_MN, have been demonstrated to exert a noteworthy influence on LST [32,67–69]. The differences in the fractions of ISA and UGS components in satellite image pixels can introduce significant interference in the direction and extent of their impact on LST. This also means that not all ISA and UGS patch landscape patterns contribute to LST changes. Previous research has shown that only patches composed of pixels with high ISA (or UGS) component fractions can significantly enhance (or mitigate) environmental temperatures [28,29]. Here, on the basics of the mean standard deviation method, the analysis zone is divided into three categories of patches based on the fractions of ISA and UGS components: high-fraction, medium-fraction, and low-fraction. Landscape metrics for high-fraction ISA (or UGS) patches within each 500 × 500 m^2 grid are calculated using the moving-window method in Fragstats 4.2. In the end, the landscape metrics are obtained for high-fraction ISA patches (LPI_{ISA}, $COHESION_{ISA}$, AI_{ISA}, and $SHAPE\_MN_{ISA}$) and high-fraction UGS patches (LPI_{UGS}, $COHESION_{UGS}$, AI_{UGS}, and $SHAPE\_MN_{UGS}$).

2.4.7. UGS Shading Index Estimation

The estimation of the UGS shading degree is primarily based on field observations of vegetation shadows, and the observed results are significantly influenced by the time of day. While there is no mature regional remote sensing estimation model for vegetation shading degree, the UGS shading index (UGSSI) can be approximated using the normalized leaf area index (*LAI*). For Landsat 8 data, multiple linear regression is recommended to represent the mathematical relation of LAI with various vegetation and soil indices (calculated using red, blue, and NIR bands) [70]. This model has been reported to have high goodness of fit ($R^2 > 0.86$) [71]. The formula is as follows:

$$UGSSI = (LAI - LAI_{min})/(LAI_{max} - LAI_{min}) \tag{14}$$

$$\begin{aligned} LAI = 1.493 \times RVI - 0.864 \times PVI - 1.964 \times SAVI_{L=0.35} - 7.378 \times MSAVI \\ +4.145 \times ARVI_{\gamma=1} + 34.396 \times ARVI_{\gamma=0.5} \\ -20.966 \times SARVI_{L^*=0.5,\ \gamma^*=1} - 1.430 \end{aligned} \tag{15}$$

where *RVI* represents the vegetation index ratio; *PVI* stands for perpendicular vegetation index; *SAVI* denotes the soil-adjusted vegetation index; *MSAVI* corresponds to the modified-soil-adjusted vegetation index; *AVI* signifies the atmospherically resistant vegetation index; *MSAVI* is the modified-soil-adjusted vegetation index; *SAVI* represents the soil-adjusted vegetation index; *MSAVI* is the modified-soil-adjusted vegetation index; *ARVI* is the atmospherically resistant vegetation index; and *SARVI* is the soil atmospherically resistant vegetation index.

2.4.8. ET Inversion

The remote sensing Penman–Menteith (RS-PM) model [72,73] is extensively employed for estimating regional ET due to its minimal requirement for meteorological parameters. However, it is generally applicable to natural surfaces dominated by vegetation and soil cover. In urban areas, remote sensing images often contain pixels that are a mixture of two or more land cover types (ISA, vegetation, and soil). Therefore, when estimating urban ET, it is necessary to first determine the mixture ratio of vegetation and soil components within mixed pixels and consider the independent surface energy balance processes of each component. The urban RS-PM model [74] addresses these requirements, rendering it apt for ET estimation in urban settings. The formula is as follows:

$$ET = \lambda ET_v + \lambda ET_s \tag{16}$$

$$\lambda ET_v = f_v \left[\frac{\Delta R^*_{n,v} + \rho C_p (e_s - e_a)/r_{ah,v}}{\Delta + \gamma \left(1 + \frac{r_{s,v}}{r_{ah,v}}\right)} \right] \tag{17}$$

$$\lambda ET_s = f_s \left[\frac{\Delta \left(R^*_{n,s} - G^*_s\right) + \rho C_p (e_s - e_a)/r_{ah,s}}{\Delta + \gamma \left(1 + \frac{r_{tot}}{r_{ah,s}}\right)} \times \left(\frac{RH}{100}\right)^{(e_s - e_a)/100} \right] \tag{18}$$

where λ represents the latent heat of vaporization of water; f_v and f_s represent the vegetation and soil fraction abundances obtained through mixed pixel decomposition; $\Delta = d(e_s)/d(T)$ is the slope of the saturation vapor pressure (e_s) curve; $R^*_{n,v}$ and $R^*_{n,s}$ represent the net radiation of pure vegetation and soil pixels, respectively; G^*_s is the heat flux of a pure soil pixel; ρ is air density; C_p is the specific heat capacity of air; e_a is the actual water vapor pressure; $r_{ah,v}$ and $r_{ah,s}$ are the aerodynamic resistances of vegetation and soil, respectively; γ is the psychrometric constant; $r_{s,v}$ is the surface resistance of the vegetation canopy; r_{tot} is the sum of surface resistance and aerodynamic resistance for water vapor evaporation; and *RH* is the relative humidity of the air.

2.5. GWR

GWR [75] fits a separate local linear regression equation for each spatial grid within a spatial range, capturing the spatially varying relationship between the numerical values of each regulating factor and LST to represent the non-stationary relationship between the independent variables X and the dependent variable Y [76]. In the GWR model, the relationship between Y and X is as follows:

$$Y_m = \beta_0(u_m, v_m) + \sum_{k=1}^{p} \beta_k(u_m, v_m) X_{mk} + \varepsilon_m \tag{19}$$

where Y_m represents the explained variable for the mth spatial unit; (u_m, v_m) represents the spatial coordinates of the mth spatial unit; $\beta_0(u_m, v_m)$ is the intercept term for the mth spatial unit; $\beta_k(u_m, v_m)$ is the regression coefficient for the kth independent variable for the mth spatial unit; X_{mk} represents the explanatory value of the kth independent variable for spatial unit m; p is the number of variables participating in the regression for spatial unit m; and ε_m is the random error term. The formula for solving the regression coefficients for each sample point within the spatial unit is as follows:

$$\beta^*(u_m, v_m) = \left[X^T W(u_m, v_m) X\right]^{-1} X^T W(u_m, v_m) Y \tag{20}$$

where $\beta^*(u_m, v_m)$ represents the estimated model parameters; X is the independent variable matrix; Y is the dependent variable matrix; and $W(u_m, v_m)$ is the spatial weight matrix for the model. A Gaussian kernel function is used as the weight function, and the spatial attenuation coefficient is calculated to form the diagonal elements of the weight matrix. The formula is as follows:

$$W_{mj} = exp\left[-(d_{mj}/b)^2\right] \tag{21}$$

where d_{mj} represents the distance between spatial unit m and j, and b is the bandwidth parameter that represents the attenuation parameter between distance and weight W_{mj}.

2.6. Bivariate Spatial Autocorrelation

Bivariate spatial autocorrelation is an extension and expansion of the univariate Moran's I index [77], which reflects the spatial clustering relationships between two different attribute variables [78]. Here, the bivariate global Moran's I index is used to indicate the overall spatial correlation and its degree between the regulating factors and LST. The equations are as follows:

$$I = \sum_{i=1}^{n} \sum_{j=1}^{n} W_{ij}(x_i - x_m)(y_j - y_m) / S^2 \sum_{i}^{n} \sum_{j=1}^{n} W_{ij} \tag{22}$$

where I represents the global spatial autocorrelation coefficient; x_i is the attribute value of spatial unit i; y_j is the attribute value of spatial unit j; x_m and y_m are the mean values of the independent and dependent variables; S^2 is the variance of the variable; and W_{ij} is the spatial weight matrix. The value of I ranges from -1 to 1, and the closer its absolute value is to 1 the stronger the spatial correlation. When I is positive, it indicates a positive correlation between the variable attributes, while when I is negative, it indicates a negative correlation.

In this study, bivariate local spatial autocorrelation was used to explore the spatial clustering characteristics of the regulating factors and LST.

$$I' = z_i \sum_{j=1}^{n} W_{ij} z_j \tag{23}$$

where I' represents the local spatial autocorrelation coefficient, and z_i and z_j are the variance-standardized values of variables for spatial units i and j, respectively. Based on I' and z-test values, the correlation between the regulating factors and LST in local regions can be classified into five types: high–high clustering, high–low clustering, low–low clustering, low–high clustering, and spatially non-significant.

2.7. Geographical Detector

Geographic Detector is a statistical model used to assess the spatial heterogeneity of influencing factors and their effects on geographical phenomena [79]. In this study, we mainly utilized the factor detection and interaction detection modules within the Geographic Detector framework. The factor detection module is employed to evaluate the contribution of each influencing factor in explaining the spatial heterogeneity of land surface temperature, which is represented by the q-value.

$$q = 1 - \frac{SSW}{SST} \tag{24}$$

$$SSW = \sum_{h=1}^{L} N_h \sigma_h^2 \tag{25}$$

$$SST = N\sigma^2 \tag{26}$$

where h = 1 to L represents the strata or layers for the variable Y or factor X, which can be categories or partitions; N_h and N are the number of units within stratum h and the total number of units in the entire area, respectively; ${\sigma_h}^2$ and σ^2 are the variances of Y values within stratum h and the total area, respectively; SSW and SST stand for the sum of squares within strata and the total sum of squares of the entire area. The q-value ranges from 0 to 1, where a higher q-value indicates a stronger explanatory power of the factor for the ecological environmental quality, while a lower q-value indicates a weaker explanatory power.

Interaction detection modules are used to identify whether two regulating factors interact with each other in influencing the dependent variable Y. In other words, when these two regulating factors act together, they may either increase or decrease their explanatory power for LST. Different types of interactions are described in Table A1 of Appendix A.

3. Results

3.1. Inversion Results of LST and Regulatory Factors

The LST inversion results based on the 500 × 500 m^2 fishnet resampling is shown in Figure 3. The average LST for four periods (from 2014 to 2018) are 33.2 °C, 35.9 °C, 32.5 °C, and 31.9 °C, respectively. Furthermore, the temperature differences between the highest and lowest temperatures for each period are 24.8 °C, 22.7 °C, 21.8 °C, and 20.0 °C, respectively. LST maps also indicate that urban built-up areas primarily covered by ISAs in the study area exhibit higher LSTs, forming pronounced heat islands. Conversely, suburban areas or water bodies dominated by vegetation cover in the study area have lower LSTs, resulting in cold islands (see the land classification results of surface cover in Figure A1 of Appendix A). The LST values for the four periods exhibit good spatial distinguishability, making them suitable for exploring the regulatory effects of various warming and cooling factors on LST spatial heterogeneity.

Compared to other regulating factors, there is a certain subjectivity in the calculation of the f_i and f_v factors during the endmember selection process in FCLS. Therefore, 100 random validation areas were selected from the GF-1 images, dated 5 October 2016, to extract the actual land surface coverage proportions within these areas and validate the FCLS results, as shown in Figure 4a and Table 3. The extracted values of f_i and f_v exhibit a strong correlation and linear fitting goodness with the true values, along with low root mean square errors (r > 0.89, R^2 > 0.80, and RMSE < 0.13).

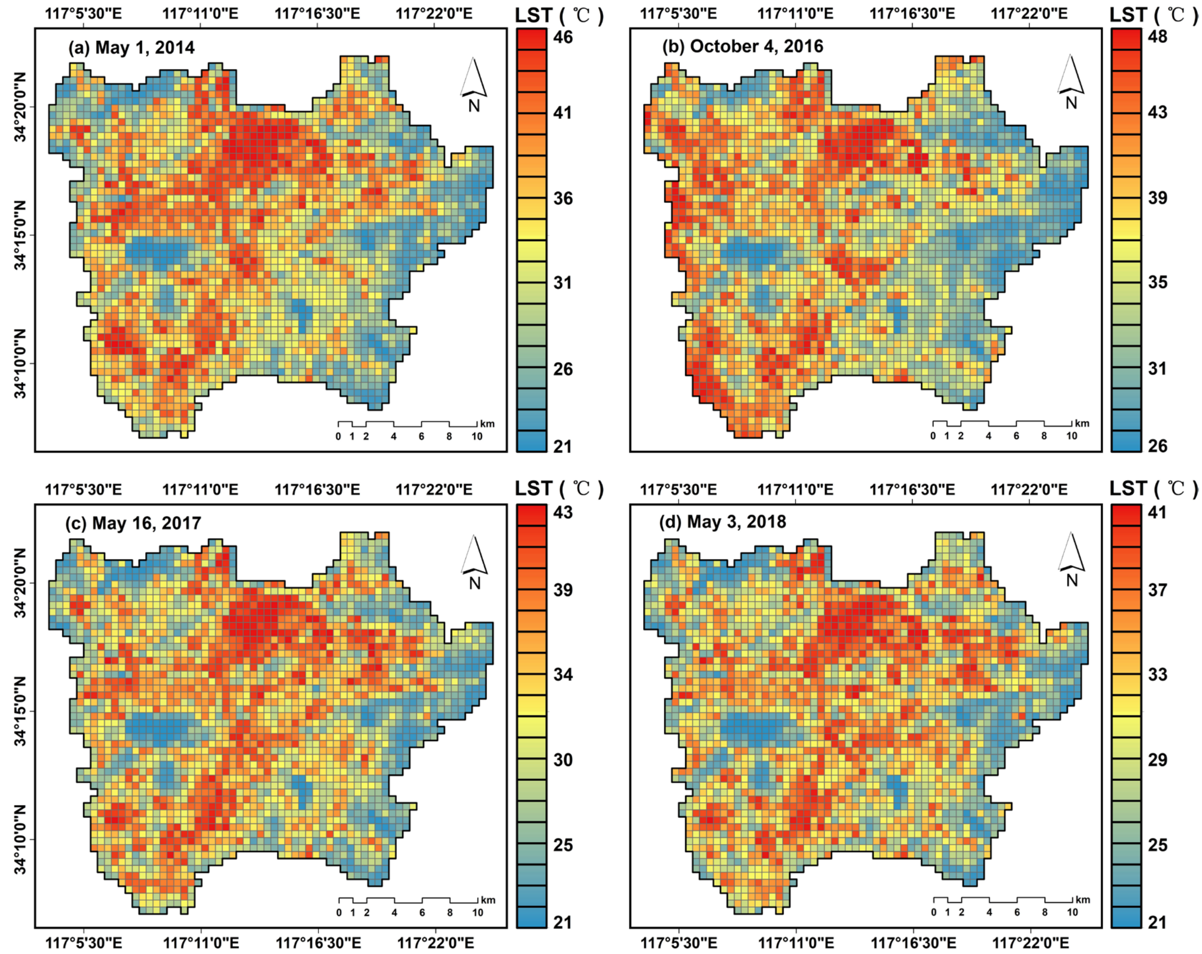

Figure 3. LST inversion results for four periods resampled based on the fishnet.

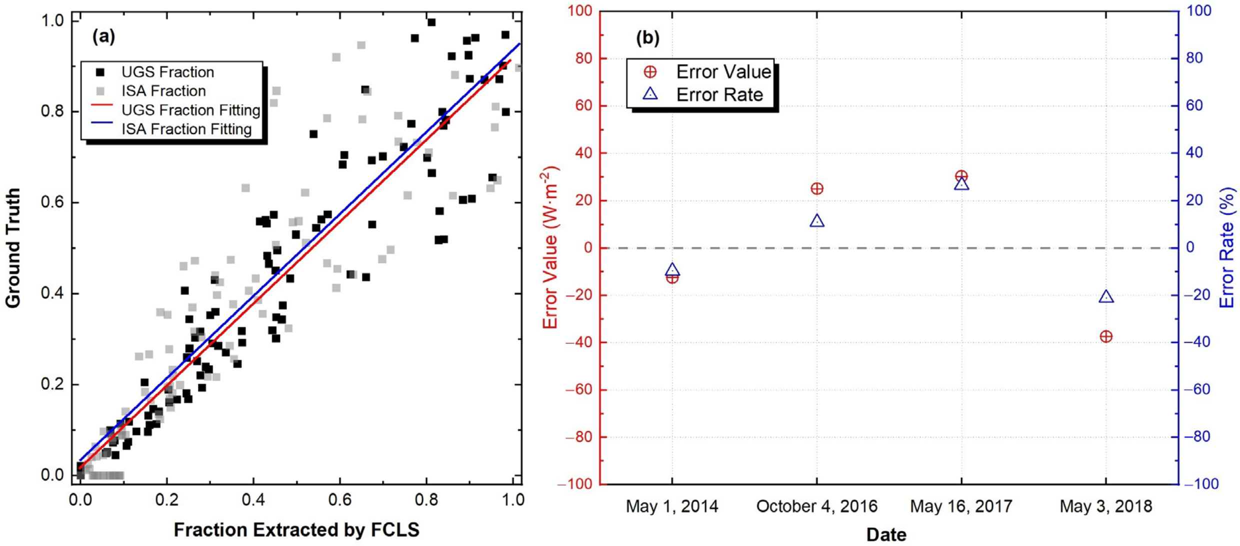

Figure 4. (**a**) Accuracy validation between FLCS endmember fraction and ground truth values; (**b**) accuracy validation between weighted λET retrieval values for the source area and EC observations.

Table 3. The accuracy verification results of UGS fraction and ISA fraction.

	UGS Fraction Fitting with Ground Truth	ISA Fraction Fitting with Ground Truth
Equation	$y = 0.902x + 0.019$	$y = 0.906x + 0.032$
Pearson r	0.931	0.894
R^2	0.866	0.800
RMSE	0.108	0.126

In addition, there are numerous intermediate parameters involved in ET inversion, making it necessary to validate the modeled ET results. Here, a footprint model [80] is employed to simulate the spatial extent (source area) of EC-observed latent heat flux within the ET inversion map. Ultimately, the weighted values of ET inversion results within the source area are calculated, allowing for a direct comparison with observed values. Figure 4b demonstrates that the errors between the four-phase EC observational values and the weighted values of the ET source area are relatively small (9.7% < ∣Error Rate∣ < 26.5%). Therefore, the accuracies of FCLS and ET inversion are acceptable for subsequent research.

After calculating and obtaining the 15 regulating factors, each regulating factor for each period is categorized into four grades, A, B, C, and D, based on their numerical values from small to large. Then, a boxplot is constructed between the regulating factor values for each grade and the corresponding LST values, as shown in Figure 5. The regulating factors including f_i, Albedo, Population, AHF, LPI_{ISA}, $COHESION_{ISA}$, AI_{ISA}, and $SHAPE\_MN_{ISA}$ generally exhibit an upward trend in their corresponding LST boxplot features (including the upper whisker, lower whisker, upper quartile, median, and lower quartile) with increasing grades. In contrast, regulating factors including f_v, ET, UGSSI, LPI_{UGS}, $COHESION_{UGS}$, AI_{UGS}, and $SHAPE\_MN_{UGS}$ generally show a downward trend in their corresponding LST box plot features with increasing grades. This phenomenon allows for an initial visual distinction between the warming or cooling attributes of all regulating factors.

3.2. GWR Results

In order to further validate and quantify the influence of each regulating factor on LST, the GWR model was applied to quantify the respective correlation and direction between each regulatory factor and LST, as shown in Figure 6. For the purpose of eliminating the magnitude differences among the regulatory factors and facilitating the comparison of their quantitative relationships with LST, all regulating factors and LST values were standardized to the [0, 1] range prior to the GWR analysis. The standardized regulating factors are labeled as follows: *R1* (normalized f_i), *R2* (normalized Albedo), *R3* (normalized Population), *R4* (normalized AHF), *R*5 (normalized LPI_{ISA}), *R6* (normalized $COHESION_{ISA}$), *R7* (normalized AI_{ISA}), *R8* (normalized $SHAPE\_MN_{ISA}$), *R9* (normalized f_v), *R10* (normalized ET), *R11* (normalized UGSSI), *R12* (normalized LPI_{UGS}), *R13* (normalized $COHESION_{UGS}$), *R14* (normalized AI_{UGS}), and *R15* (normalized $SHAPE\_MN_{UGS}$).

Figure 6a shows that the GWR global goodness-of-fit R^2 values between all regulating factors and LST for the four periods range from 0.64 to 0.91, indicating strong correlations across the board. Furthermore, we extracted the GWR coefficients of each regulating factor for all grids and calculated their average value. The average GWR coefficients between *R1* to *R8* and LST are positive, whereas those between *R9* to *R15* are negative, as illustrated in Figure 6b. Consequently, *R1* to *R8* can be categorized as warming factors, while *R9* to *R15* can be categorized as cooling factors. Although R^2 and the average regression coefficients can quantify the correlation degree between each regulating factor and LST, the GWR method calculates the relationship between each factor and LST independently, without considering the combined influence of all factors on LST. Therefore, the results of GWR cannot directly represent the contribution of each regulating factor to LST.

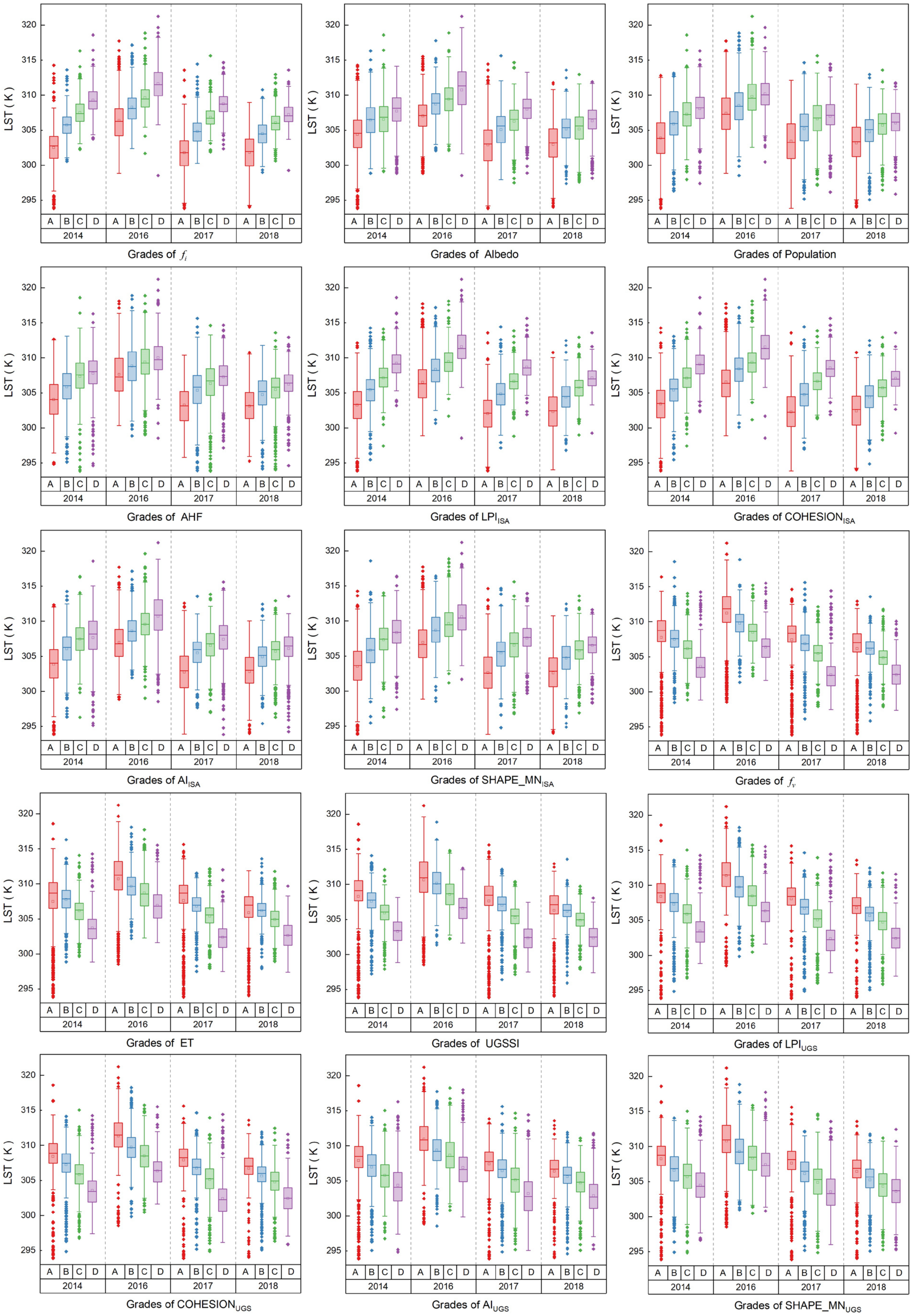

Figure 5. LST box plots corresponding to four levels of the regulatory factors grouped in four periods (A, B, C and D are the four grades from small to large based on the values of each factor).

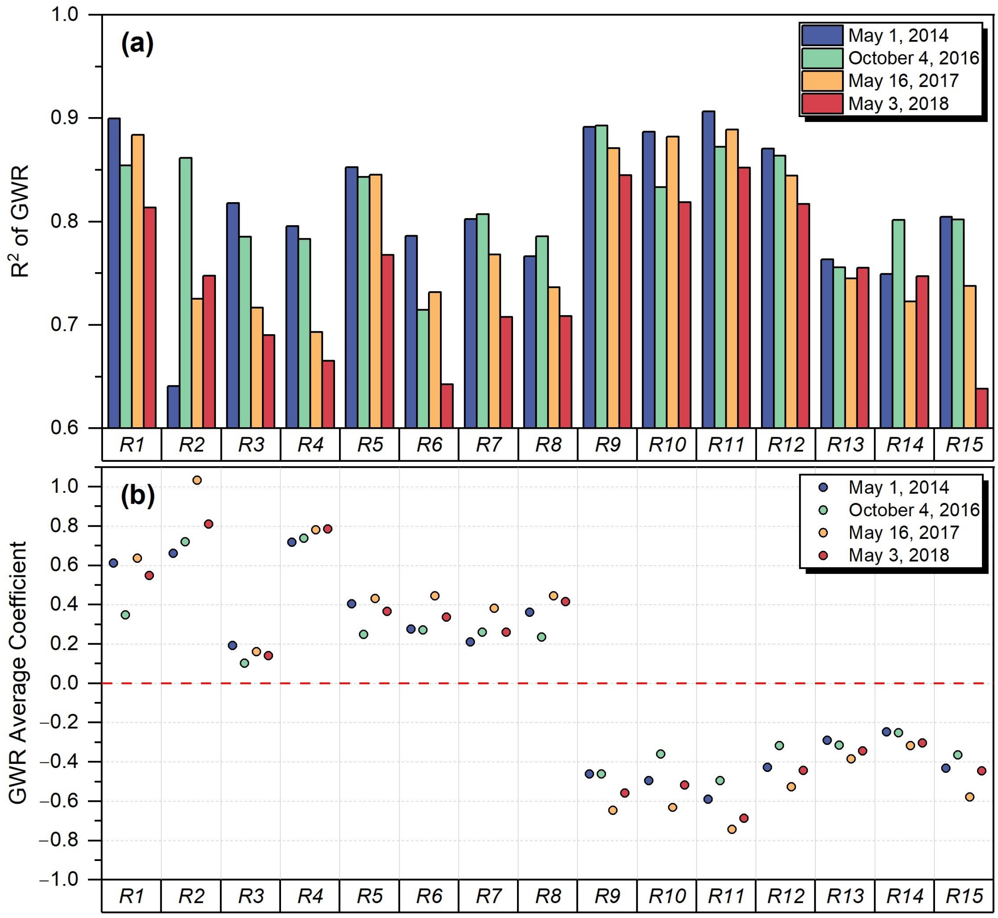

Figure 6. (**a**) Global fitting goodness R^2 and (**b**) average coefficient of GWR.

3.3. Bivariate Spatial Autocorrelation Results

The bivariate global Moran's I (Figure 7) illustrates the extent and direction of spatial correlations between regulatory factors and LST. Warming factors all exhibit a significant positive spatial correlation with LST ($p < 0.001$). Among them, the average Moran's I of f_i and Population are 0.44 and 0.15, respectively, which represent the maximum and minimum values. This indicates that ISA density is the warming factor with the strongest spatial correlation to LST, while Population is the warming factor with the weakest spatial correlation to LST. Additionally, the average Moran's I for AHF is higher than that of Albedo.

The cooling factors all exhibit significant spatial negative correlations with LST ($p < 0.001$). Among them, the average Moran's I of UGSSI and SHAPE_MN$_{UGS}$ are -0.49 and -0.25, respectively, which are the maximum and minimum values (in absolute terms). This indicates that vegetation shadow is the cooling factor with the strongest spatial correlation to LST, while the shape index of UGS patches is the cooling factor with the weakest spatial correlation to LST. Furthermore, the average Moran's I values for f_v and ET are both 0.45, suggesting that their spatial correlations with LST are very close.

Another prominent pattern is the spatial correlation strength between the landscape metrics of LSTs and ISAs or UGSs, which follow a descending order as LPI, COHESION, AI, and SHAPE_MN. This indicates that the maximum patch size of ISAs or UGSs within the region is the primary landscape factor influencing the spatial heterogeneity of LST.

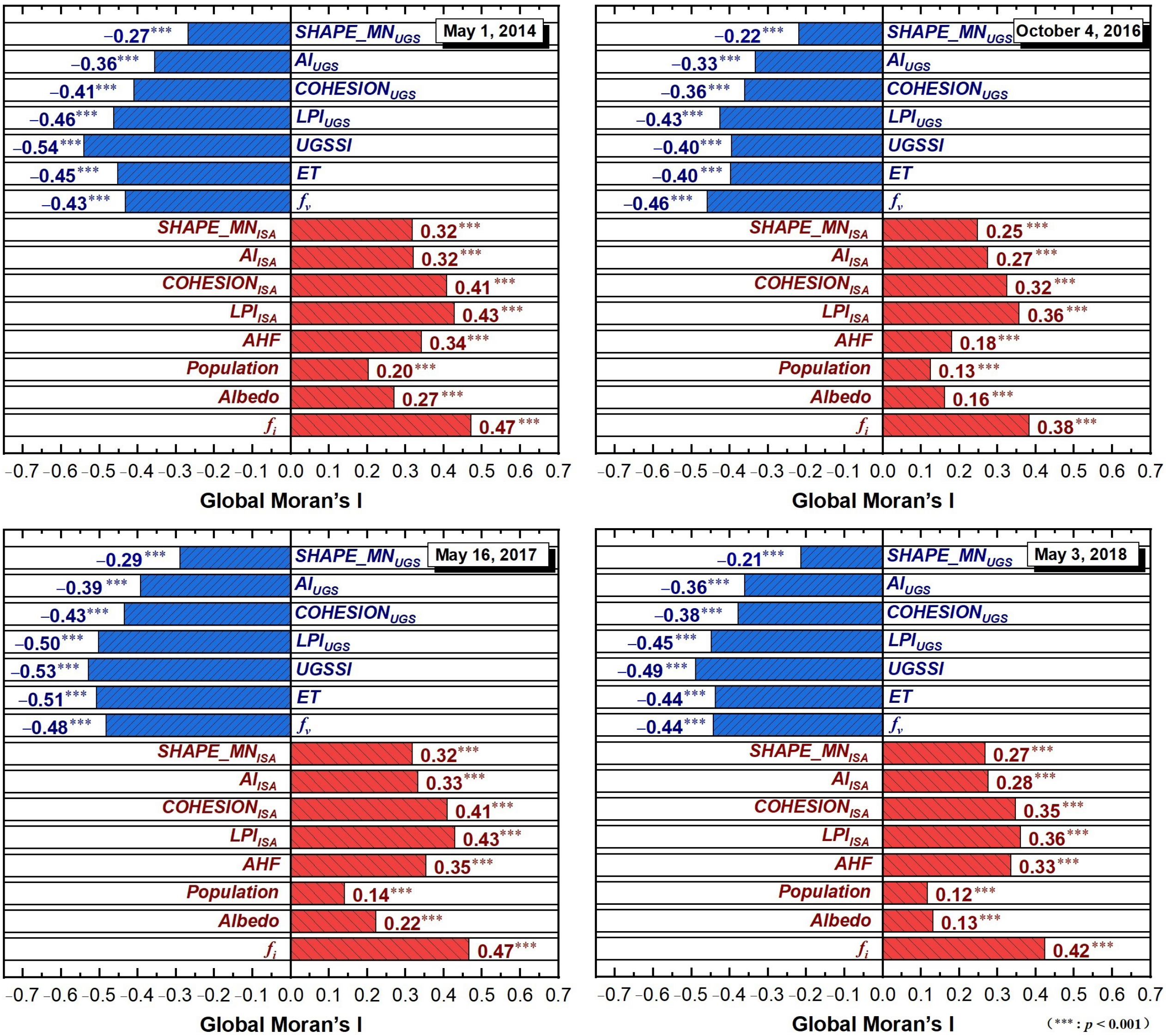

Figure 7. Global Moran's I between LST and regulatory factors for four periods (red and blue represent positive and negative spatial correlations, respectively).

Taking the results of the bivariate local Moran's I for 1 May 2014 as an example, the spatial associations between regulating factors and LST are shown in local indicators of spatial association (LISA) maps (Figure 8). For warming factors, their spatial distribution patterns with LST are predominantly characterized by high LST-high warming factor (H-H) and low LST-low warming factor (L-L) clusters, with H-H clusters mostly found in urban built-up areas and L-L clusters primarily distributed in urban forests and suburban farmlands. On the other hand, the spatial distribution patterns of cooling factors with LST are dominated by H-L and L-H clusters, where H-L cluster types are predominantly found in vegetation-rich regions, while L-H cluster types are mostly covered by impervious surfaces.

3.4. Geographical Detector Results

3.4.1. Factor Detection

The factor detection of Geographic Detector results (Table 4) show that almost all regulating factors have significant driving effects on LST in four periods ($p < 0.001$), and their contribution levels (q) vary significantly. For warming factors (*R1* to *R8*), *R1* (f_i) has the highest contribution level to urban LST (average $q = 0.51$), indicating that ISA density has the highest impact weight on urban warming. On the other hand, *R3* (Population) has the lowest contribution level to LST (average $q = 0.04$), and its contributions to LST on 4 October 2016 and 3 May 2018 are not significant ($p > 0.05$), suggesting that population density is not a core factor influencing the urban thermal environment. Furthermore, the contribution levels of *R5* to *R8* ($0.42 \geq$ average $q \geq 0.24$) are significantly greater than those of *R2* to *R4* ($0.16 \geq$ average $q \geq 0.04$). This indicates that the spatial patterns of ISA patches are also crucial factors driving urban warming, especially *R5* (LPI_{ISA}) and *R6* ($COHESION_{ISA}$) with average q-values of 0.42 and 0.39, respectively.

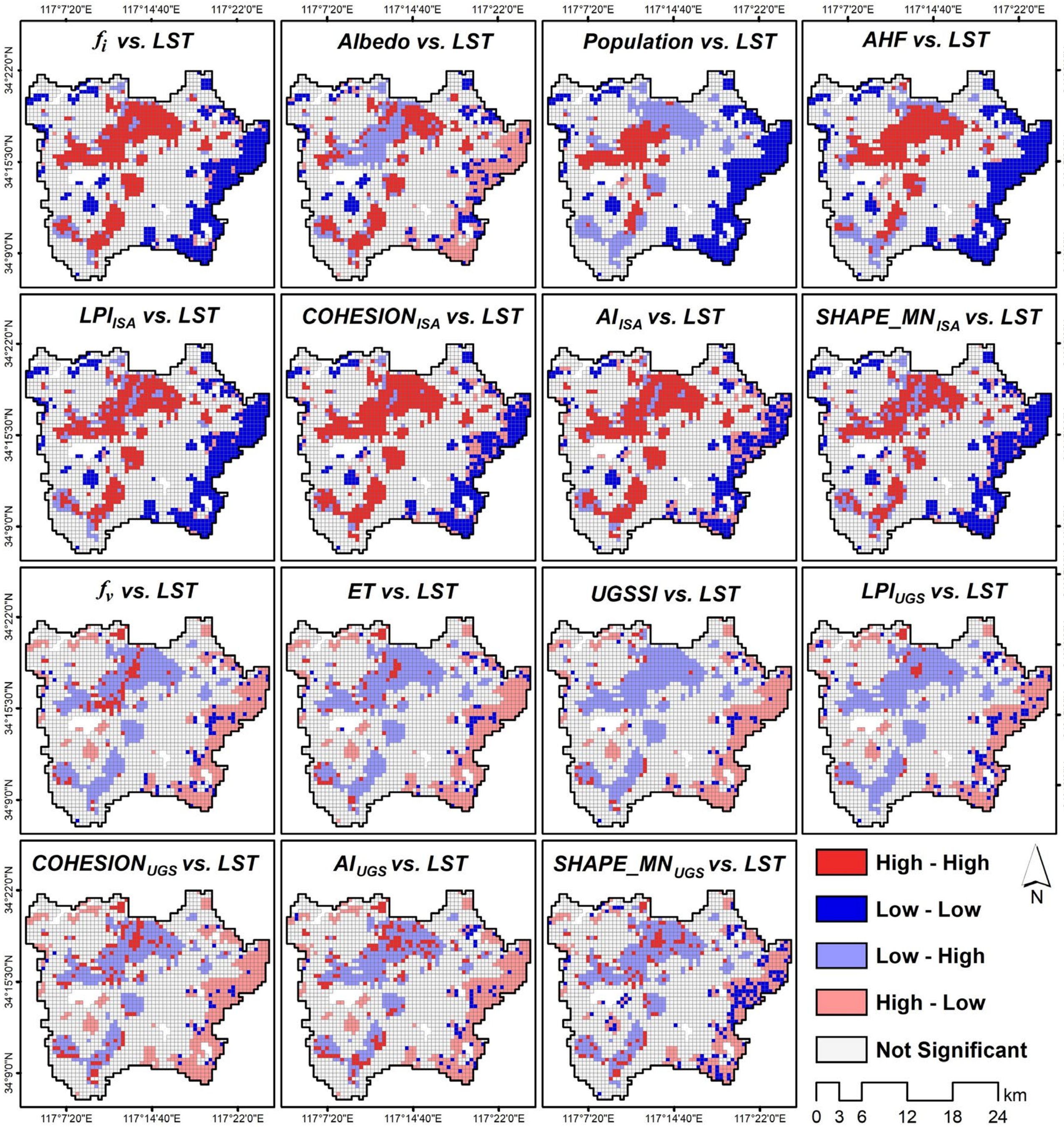

Figure 8. Local indicators of spatial association (LISA) cluster distribution maps between LST and regulatory factors (taking the results from 1 May 2014 as an example).

Table 4. Results of the detection of urban LST driving factors.

Factor	1 May 2014		4 October 2016		16 May 2017		3 May 2018	
	q	*p*	*q*	*p*	*q*	*p*	*q*	*p*
R1 (f_i)	0.59	0.000	0.37	0.000	0.60	0.000	0.49	0.000
R2 (Albedo)	0.09	0.000	0.16	0.000	0.26	0.000	0.14	0.000
R3 (Population)	0.07	0.000	0.03	0.748	0.04	0.012	0.03	0.424
R4 (AHF)	0.21	0.000	0.07	0.000	0.19	0.000	0.18	0.000
R5 (LPI_{ISA})	0.44	0.000	0.35	0.000	0.54	0.000	0.38	0.000
R6 ($COHESION_{ISA}$)	0.42	0.000	0.28	0.000	0.49	0.000	0.36	0.000
R7 (AI_{ISA})	0.25	0.000	0.21	0.000	0.32	0.000	0.22	0.000
R8 ($SHAPE\_MN_{ISA}$)	0.28	0.000	0.17	0.000	0.27	0.000	0.22	0.000
R9 (f_v)	0.53	0.000	0.55	0.000	0.63	0.000	0.59	0.000
R10 (ET)	0.52	0.000	0.39	0.000	0.69	0.000	0.54	0.000
R11 (UGSSI)	0.67	0.000	0.41	0.000	0.69	0.000	0.64	0.000
R12 (LPI_{UGS})	0.55	0.000	0.47	0.000	0.62	0.000	0.57	0.000
R13 ($COHESION_{UGS}$)	0.49	0.000	0.42	0.000	0.56	0.000	0.48	0.000
R14 (AI_{UGS})	0.32	0.000	0.30	0.000	0.38	0.000	0.36	0.000
R15 ($SHAPE\_MN_{UGS}$)	0.22	0.000	0.16	0.000	0.26	0.000	0.17	0.000

For cooling factors (*R9* to *R15*), *R11* (UGSSI) has the highest contribution level to urban LST (average q = 0.60), indicating that impervious surface density has the highest impact weight on urban cooling. On the other hand, the influence weight of *R15* ($SHAPE\_MN_{UGS}$) is the lowest. Another observation is that the contribution levels of *R9* to *R11* (0.60 $\geq$ average q $\geq$ 0.53) are generally higher than those of *R12* to *R15* (0.55 $\geq$ average q $\geq$ 0.20). This suggests that, compared to the spatial patterns of UGS patches, vegetation density, heat-water exchange, and vegetation shading are more effective in mitigating LST.

By comprehensively comparing the contribution levels of warming and cooling factors to LST across the four periods, we observe a trend where cooling factors contribute more significantly than warming factors. There are four cooling factors (*R9* to *R12*) with an average q above 0.5, whereas there is only one warming factor (*R1*). This suggests that improving UGSs is a more effective approach for mitigating the urban thermal environment. Another observation is that the contribution levels of the landscape patterns of ISAs and UGSs to LST can all be ranked as LPI > COHESION > AI > SHAPE_MN. Therefore, reshaping the regional maximum patch area and enhancing the connectivity between patches of ISAs (or UGSs) are effective ways to reduce environmental temperature.

3.4.2. Interaction Detection

The results of interaction detection between each pair of driving factors are mapped onto a heatmap (Figure 9); it was observed that all factor pairs exhibited a nonlinear enhancing effect on LST. This indicates that the interactions between any two of the 15 selected regulating factors can exert a stronger driving force on LST, emphasizing that the interactions among factors are more capable of explaining the spatial distribution characteristics of LST.

Using Figure 9a as a reference, the heatmaps for the four periods were classified into three regions representing interactions between warming factors (Region A), interactions between cooling factors (Region B), and interactions between warming and cooling factors (Region C). In each of these regions (A, B, and C), we selected three pairs of factors with the highest q-values and recorded their frequency of occurrence across the four periods. The results show that there are six pairs of factor combinations with the highest frequency of occurrence, indicating that these combinations have the strongest explanatory power for LST in the three Regions A, B, and C, respectively. In Region A, *R1* $\cap$ *R2* (average q = 0.600) and *R1* $\cap$ *R7* (average q = 0.584) have a relatively high frequency of occurrence and the lowest q-values among the three regions. This suggests that, while reducing ISA density in a particular area, combining it with the use of low albedo ISA materials or reducing the aggregation level of ISA patches can be even more effective in mitigating the urban thermal environment. In Region B, *R11* ∩ *R9* (average $q = 0.700$) and *R11* ∩ *R12* (average $q = 0.696$) have the highest frequency of occurrence and relatively higher q-values among the three regions. This suggests that increasing broadleaf vegetation to expand the urban shading area while simultaneously increasing UGS density or increasing the size of the largest UGS patches in the area is a better approach to urban cooling. In Region C, *R1* ∩ *R11* (average $q = 0.702$) and *R2* ∩ *R11* (average $q = 0.705$) have the highest frequency of occurrence and the highest q-values among the three regions. This indicates that increasing the UGS shading area while combining it with the use of low albedo ISA materials or reducing ISA density is the most effective way to control urban LST.

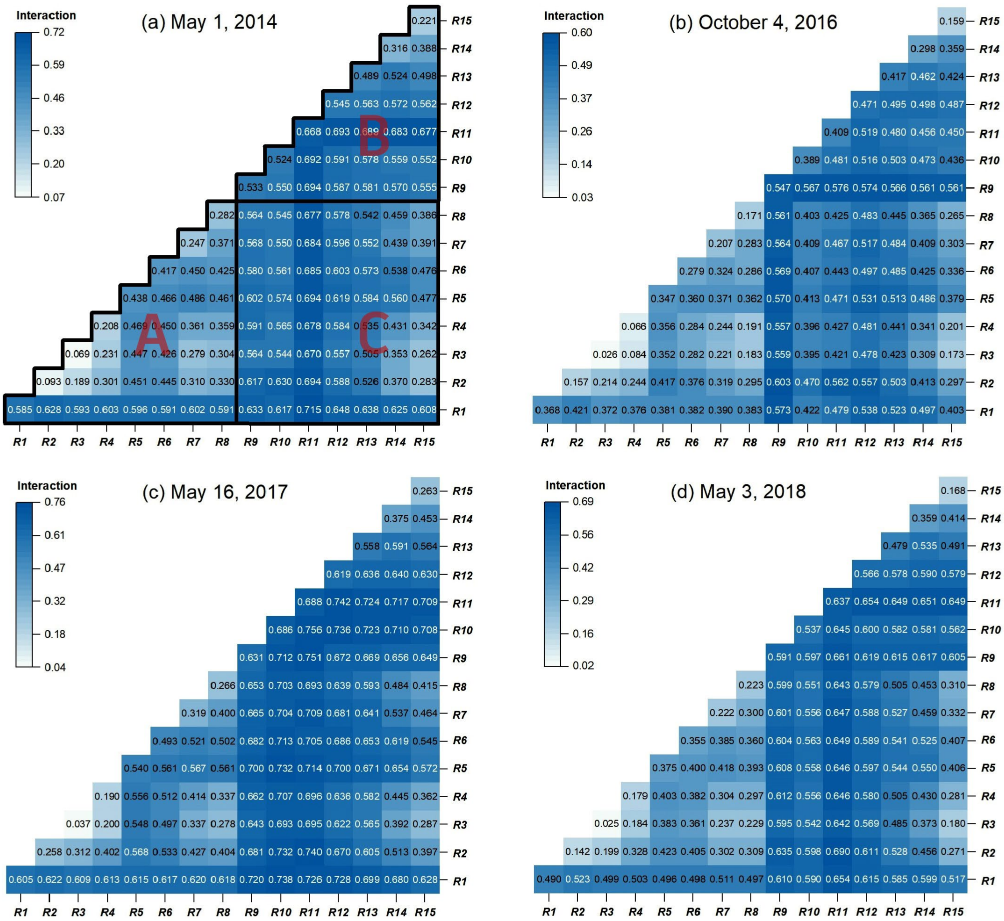

Figure 9. Interaction detection results of urban LST driving factors (A, B and C representing interactions between warming factors, interactions between cooling factors, and interactions between warming and cooling factors, respectively).

4. Discussion

The primary reason for urban LST being higher than those in the surrounding suburbs is the replacement of ISAs, thereby altering the heat conduction and storage characteristics of the land. Research has found a correlation coefficient of 0.82 between the proportion of regional ISAs and daily average temperatures [42], and our study similarly found that the R^2 of GWR between ISA density and LST ranges from 0.81 to 0.90.

Land surface albedo has been reported to have a significant correlation with LST (Pearson $r = 0.231$, $p < 0.01$) [43], which is also supported by our results. Additionally, we have found that the combination of UGSSI and Albedo provides the strongest explanatory power for LST.

Residential areas with high population density in urban areas are often associated with urban hotspots and heat extremes [44,45], with correlation coefficients of 0.42 and

0.70 during normal summer conditions at around 12:30 and 01:30, respectively [44]. This phenomenon has also been confirmed in our study. However, we have also found that while population is strongly correlated with urban LST (average GWR $R^2 > 0.75$), its contribution to LST is the lowest among all the regulating factors (average $q = 0.04$).

AHF serves as a substantial contributor to urban warming. Simulation data from major cities like Los Angeles, Atlanta, and Beijing have shown that estimated anthropogenic surface temperatures (ALST) generated by AHF range from 1.99 to 2.99 °C [46]. Additionally, research has reported a fairly high correlation between AHF and LST (Pearson r = 0.357, $p < 0.01$) [43]. Our study also confirms the positive association between AHF and LST and further elucidates the spatial correlation and contribution of AHF to LST (average $q = 0.16$).

Some studies have revealed that vegetation density and ET have a strong mitigating effect on the urban thermal environment, with absolute correlation coefficients with LST exceeding 0.60 ($p < 0.001$) [28,49,50]. This is consistent with our results. We used the standardized LAI as a representation of the UGS shading degree, primarily based on previous research findings that a larger tree canopy coverage leads to stronger cooling effects [24]. Our findings not only confirm the significant negative relationship between UGSSI and environment temperature, which aligns with previous studies [24,51], but also reveal that it has the highest contribution to LST (average $q = 0.60$).

The impact weights of landscape patterns on LST have been revealed. However, the landscape metrics for ISA patches and UGS patches were investigated independently. For ISA patches, previous research has shown that the contribution weights of various landscape indices to LST can be ranked from highest to lowest as PLAND, COHESION, LPI, and AI [29]. Among these indices, PLAND represents the proportion of ISA patches in the area, and the meaning of the index f_i we selected in our study also represents the density of ISA patches within the region. Therefore, this result is generally consistent with the order we investigated, which is f_i, $\mathrm{LPI_{ISA}}$, $\mathrm{COHESION_{ISA}}$, and $\mathrm{AI_{ISA}}$. However, there is a difference in the weight ranking between COHESION and LPI in our study compared to previous research. Regarding UGS patches, previous research has indicated that the impact weights of their landscape indices on LST can be arranged from highest to lowest as PLAND, COHESION, LPI, and AI [28]. This aligns with our study results, where a similar order of f_v, $\mathrm{LPI_{UGS}}$, $\mathrm{COHESION_{UGS}}$, $\mathrm{AI_{UGS}}$ is generally consistent. The sole difference also lies in the contribution ranking between LPI and COHESION. The main discrepancies mentioned above are primarily due to two reasons. Firstly, previous research conducted separate analyses of the impact weights of landscape indices for ISA patches (or UGS patches) on LST, where all indices had either a positive or negative impact on LST. In contrast, our study comprehensively considers the combined effects of 15 warming and cooling factors, where factors can have both positive and negative impacts on LST. This difference can influence the construction of the mathematical model for calculating contribution rates. Secondly, there is a potential reason related to the methodology. Previous studies used a combination of principal component analysis (PCA) and multiple linear regression when calculating contribution rates. The core of this method lies in using the standardized regression coefficients between the reduced principal component factors and LST as the source of contribution weights. In contrast, our study used Geographic Detector to calculate the contribution weights of each factor based on the spatial variability consistency between each factor and LST. Therefore, differences in the underlying mathematical models for contribution weights may also contribute to the slight discrepancies between our results and previous research.

Furthermore, concerning the relationship between the UHI effect and vegetation or ISAs, previous research has demonstrated that urban greening has a greater potential for alleviating the UHI effect compared to building materials [81]. We also found that UGSs contribute more significantly to reducing LST compared to ISAs. Therefore, it is recommended to prioritize adjusting the attributes of UGSs to lower environmental temperatures.

5. Conclusions

Compared to traditional urban thermal environment impact investigations that focus only on individual or a few factors, we selected 15 potential positive and negative influencing factors in urban areas based on multi-source remote sensing data. These factors were chosen from five aspects: land cover density, land surface spectral characteristics, human activities, vegetation physical properties, and the spatial pattern of land patches. This improvement allows for a more comprehensive exploration of their mathematical and spatial effects on LST in scenarios where warming and cooling variables coexist. More importantly, by evaluating the contribution of each factor to land surface temperature (LST) within the context of their collective impact, we have innovatively unveiled the ranking of contributions of all warming and cooling factors. Furthermore, we have demonstrated the additive effects of their pairwise interactions on LST contributions and proposed the most effective and economically viable combinations of factors for mitigating the urban heat island (UHI) effect. The specific conclusions are as follows:

Eight arming factors and seven cooling factors exhibit significant statistical and spatial positive and negative correlations with LST, respectively. Additionally, f_i and UGSSI exhibited the highest correlations among warming and cooling factors, respectively.

The contribution of each regulatory factor to LST can be arranged from greatest to least contribution as follows: UGSSI > f_v > $\mathrm{LPI_{UGS}}$ > ET > f_i > $\mathrm{COHESION_{UGS}}$ > $\mathrm{LPI_{ISA}}$ > $\mathrm{COHESION_{ISA}}$ > $\mathrm{AI_{UGS}}$ > $\mathrm{AI_{ISA}}$ > $\mathrm{SHAPE\_MN_{ISA}}$ > $\mathrm{SHAPE\_MN_{UGS}}$ > Albedo > AHF > Population. This indicates that cooling factors, on the whole, have a higher contribution to LST reduction than warming factors. Therefore, it is recommended to prioritize the improvement of vegetation characteristics to alleviate the urban thermal environment.

The combinations $f_i \cap$ Albedo and $f_i \cap \mathrm{LPI_{ISA}}$, UGSSI $\cap f_v$ and UGSSI $\cap$ $\mathrm{LPI_{UGS, and}}$ f_i $\cap$ UGSSI and Albedo $\cap$ UGSSI are the combinations with the highest contribution weights among warming factor interactions, cooling factor interactions, and warming–cooling factor interactions, respectively. Particularly, the combination of increasing urban green space shading area with the use of low albedo building materials or reducing ISA density proves to be the most effective approach to reduce urban LST. Therefore, our results also provide valuable combinations of warming and cooling factors as references, offering cost-effective solutions for mitigating the urban heat environment.

This study has a rich variety of data sources, and different types of data exhibit certain differences in spatial and temporal resolution, especially mobile signaling data. Due to concerns regarding user privacy and security, we were only able to obtain population annual spatial distribution maps. This may lead to some errors in the study's results. Future research could rely on unmanned aerial vehicles (UAV) and light detection and ranging (LiDAR) technology to obtain more precise urban spatial data and thermal infrared data, allowing for a more detailed exploration of the regulatory effects of factors such as urban building materials, vegetation types, and the three-dimensional urban spatial structure on the thermal environment. Additionally, it can further uncover the interactions among various LST regulatory variables.

Author Contributions: Conceptualization, Y.W. and Y.Z.; methodology, Y.W.; software, Y.Z.; validation, Y.W.; formal analysis, N.D.; data curation, N.D.; writing—original draft preparation, Y.W.; writing—review and editing, Y.Z. and N.D.; visualization, N.D.; supervision, N.D.; funding acquisition, Y.W. All authors have read and agreed to the published version of the manuscript.

Funding: This research was funded by the National Natural Science Foundation of China, Grant No. 42101049.

Data Availability Statement: Not applicable.

Acknowledgments: The comments and suggestions of the editor and the anonymous reviewers are gratefully acknowledged.

Conflicts of Interest: The authors declare no conflict of interest.

Appendix A

Table A1. Interaction detection result description.

Criterion	Interaction Type
$q(X1 \cap X2) < min[q(X1), q(X2)]$	Nonlinear Attenuation
$min[q(X1), q(X2)] < q(X1 \cap X2) < max[q(X1), q(X2)]$	Single Factor Nonlinear Attenuation
$q(X1 \cap X2) > max[q(X1), q(X2)]$	Double Factor Enhancement
$q(X1 \cap X2) = q(X1) + q(X2)$	Independence
$q(X1 \cap X2) > q(X1) + q(X2)$	Nonlinear Enhancement

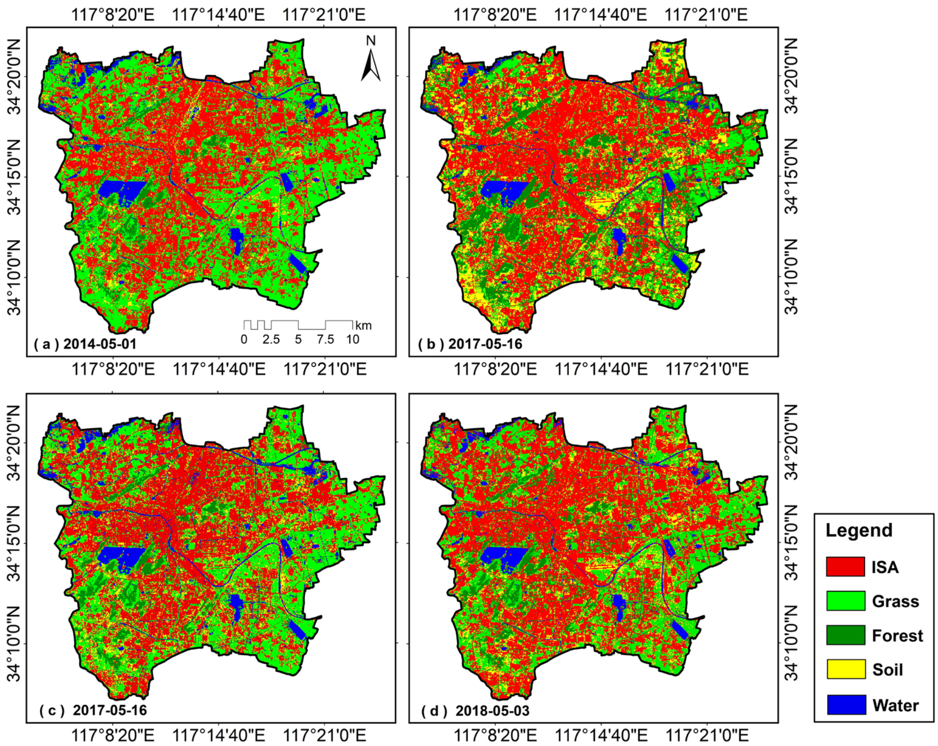

Figure A1. Land cover classification maps of four periods.

References

1. Stehfest, E.; van Zeist, W.-J.; Valin, H.; Havlik, P.; Popp, A.; Kyle, P.; Tabeau, A.; Mason-D'Croz, D.; Hasegawa, T.; Bodirsky, B.L.; et al. Key Determinants of Global Land-Use Projections. *Nat. Commun.* **2019**, *10*, 2166. [CrossRef] [PubMed]
2. Donateo, A.; Palusci, O.; Pappaccogli, G.; Esposito, A.; Martilli, A.; Santiago, J.L.; Buccolieri, R. Analysis of Urban Heat Island and Human Thermal Comfort in a Mediterranean City: A Case Study of Lecce (Italy). *Sustain. Cities Soc.* **2023**, *98*, 104849. [CrossRef]
3. Ouyang, Z.; Sciusco, P.; Jiao, T.; Feron, S.; Lei, C.; Li, F.; John, R.; Fan, P.; Li, X.; Williams, C.A.; et al. Albedo Changes Caused by Future Urbanization Contribute to Global Warming. *Nat. Commun.* **2022**, *13*, 3800. [CrossRef] [PubMed]
4. Chen, G.; Chen, Y.; Tan, X.; Zhao, L.; Cai, Y.; Li, L. Assessing the Urban Heat Island Effect of Different Local Climate Zones in Guangzhou, China. *Build. Environ.* **2023**, *244*, 110770. [CrossRef]
5. Singh, M.; Sharston, R. Quantifying the Dualistic Nature of Urban Heat Island Effect (UHI) on Building Energy Consumption. *Energy Build.* **2022**, *255*, 111649. [CrossRef]
6. Zhang, X.; Yan, F.; Liu, H.; Qiao, Z. Towards Low Carbon Cities: A Machine Learning Method for Predicting Urban Blocks Carbon Emissions (UBCE) Based on Built Environment Factors (BEF) in Changxing City, China. *Sustain. Cities Soc.* **2021**, *69*, 102875. [CrossRef]
7. Liang, Z.; Huang, J.; Wang, Y.; Wei, F.; Wu, S.; Jiang, H.; Zhang, X.; Li, S. The Mediating Effect of Air Pollution in the Impacts of Urban Form on Nighttime Urban Heat Island Intensity. *Sustain. Cities Soc.* **2021**, *74*, 102985. [CrossRef]
8. Ellena, M.; Melis, G.; Zengarini, N.; Di Gangi, E.; Ricciardi, G.; Mercogliano, P.; Costa, G. Micro-Scale UHI Risk Assessment on the Heat-Health Nexus within Cities by Looking at Socio-Economic Factors and Built Environment Characteristics: The Turin Case Study (Italy). *Urban Clim.* **2023**, *49*, 101514. [CrossRef]

9. Ren, J.; Yang, J.; Zhang, Y.; Xiao, X.; Xia, J.C.; Li, X.; Wang, S. Exploring Thermal Comfort of Urban Buildings Based on Local Climate Zones. *J. Clean. Prod.* **2022**, *340*, 130744. [CrossRef]
10. Li, X.; Zhou, Y.; Yu, S.; Jia, G.; Li, H.; Li, W. Urban Heat Island Impacts on Building Energy Consumption: A Review of Approaches and Findings. *Energy* **2019**, *174*, 407–419. [CrossRef]
11. Xi, C.; Han, L.; Wang, J.; Feng, Z.; Kumar, P.; Cao, S.-J. How Can Greenery Space Mitigate Urban Heat Island? An Analysis of Cooling Effect, Carbon Sequestration, and Nurturing Cost at the Street Scale. *J. Clean. Prod.* **2023**, *419*, 138230. [CrossRef]
12. Santamouris, M.; Cartalis, C.; Synnefa, A.; Kolokotsa, D. On the Impact of Urban Heat Island and Global Warming on the Power Demand and Electricity Consumption of Buildings—A Review. *Energy Build.* **2015**, *98*, 119–124. [CrossRef]
13. Gober, P.; Brazel, A.; Quay, R.; Myint, S.; Grossman-Clarke, S.; Miller, A.; Rossi, S. Using Watered Landscapes to Manipulate Urban Heat Island Effects: How Much Water Will It Take to Cool Phoenix? *J. Am. Plan. Assoc.* **2009**, *76*, 109–121. [CrossRef]
14. Garuma, G.F. Tropical Surface Urban Heat Islands in East Africa. *Sci. Rep.* **2023**, *13*, 4509. [CrossRef]
15. Jin, K.; Wang, F.; Chen, D.; Liu, H.; Ding, W.; Shi, S. A New Global Gridded Anthropogenic Heat Flux Dataset with High Spatial Resolution and Long-Term Time Series. *Sci. Data* **2019**, *6*, 139. [CrossRef] [PubMed]
16. Zhang, G.J.; Cai, M.; Hu, A. Energy Consumption and the Unexplained Winter Warming over Northern Asia and North America. *Nat. Clim. Chang.* **2013**, *3*, 466–470. [CrossRef]
17. Ichinose, T.; Shimodozono, K.; Hanaki, K. Impact of Anthropogenic Heat on Urban Climate in Tokyo. *Atmos. Environ.* **1999**, *33*, 3897–3909. [CrossRef]
18. Zhang, N.; Wang, X.; Chen, Y.; Dai, W.; Wang, X. Numerical Simulations on Influence of Urban Land Cover Expansion and Anthropogenic Heat Release on Urban Meteorological Environment in Pearl River Delta. *Theor. Appl. Climatol.* **2016**, *126*, 469–479. [CrossRef]
19. Ke, X.; Men, H.; Zhou, T.; Li, Z.; Zhu, F. Variance of the Impact of Urban Green Space on the Urban Heat Island Effect among Different Urban Functional Zones: A Case Study in Wuhan. *Urban For. Urban Green.* **2021**, *62*, 127159. [CrossRef]
20. Chen, X.; Wang, Z.; Bao, Y. Cool Island Effects of Urban Remnant Natural Mountains for Cooling Communities: A Case Study of Guiyang, China. *Sustain. Cities Soc.* **2021**, *71*, 102983. [CrossRef]
21. Wong, N.H.; Tan, C.L.; Kolokotsa, D.D.; Takebayashi, H. Greenery as a Mitigation and Adaptation Strategy to Urban Heat. *Nat. Rev. Earth Environ.* **2021**, *2*, 166–181. [CrossRef]
22. Morakinyo, T.E.; Dahanayake, K.W.D.K.C.; Adegun, O.B.; Balogun, A.A. Modelling the Effect of Tree-Shading on Summer Indoor and Outdoor Thermal Condition of Two Similar Buildings in a Nigerian University. *Energy Build.* **2016**, *130*, 721–732. [CrossRef]
23. Armson, D.; Stringer, P.; Ennos, A.R. The Effect of Tree Shade and Grass on Surface and Globe Temperatures in an Urban Area. *Urban For. Urban Green.* **2012**, *11*, 245–255. [CrossRef]
24. Yu, Q.; Ji, W.; Pu, R.; Landry, S.; Acheampong, M.; O' Neil-Dunne, J.; Ren, Z.; Tanim, S.H. A Preliminary Exploration of the Cooling Effect of Tree Shade in Urban Landscapes. *Int. J. Appl. Earth Obs. Geoinf.* **2020**, *92*, 102161. [CrossRef]
25. Ding, N.; Zhang, Y.; Wang, Y.; Chen, L.; Qin, K.; Yang, X. Effect of Landscape Pattern of Urban Surface Evapotranspiration on Land Surface Temperature. *Urban Clim.* **2023**, *49*, 101540. [CrossRef]
26. Wang, Y.; Zhang, Y.; Ding, N.; Qin, K.; Yang, X. Simulating the Impact of Urban Surface Evapotranspiration on the Urban Heat Island Effect Using the Modified RS-PM Model: A Case Study of Xuzhou, China. *Remote Sens.* **2020**, *12*, 578. [CrossRef]
27. Li, J.; Sun, R.; Liu, T.; Xie, W.; Chen, L. Prediction Models of Urban Heat Island Based on Landscape Patterns and Anthropogenic Heat Dynamics. *Landsc. Ecol.* **2021**, *36*, 1801–1815. [CrossRef]
28. Zhang, Y.; Wang, Y.; Ding, N. Spatial Effects of Landscape Patterns of Urban Patches with Different Vegetation Fractions on Urban Thermal Environment. *Remote Sens.* **2022**, *14*, 5684. [CrossRef]
29. Zhang, Y.; Wang, Y.; Ding, N.; Yang, X. Spatial Pattern Impact of Impervious Surface Density on Urban Heat Island Effect: A Case Study in Xuzhou, China. *Land* **2022**, *11*, 2135. [CrossRef]
30. Wang, Q.; Wang, X.; Zhou, Y.; Liu, D.; Wang, H. The Dominant Factors and Influence of Urban Characteristics on Land Surface Temperature Using Random Forest Algorithm. *Sustain. Cities Soc.* **2022**, *79*, 103722. [CrossRef]
31. Song, Z.; Yang, H.; Huang, X.; Yu, W.; Huang, J.; Ma, M. The Spatiotemporal Pattern and Influencing Factors of Land Surface Temperature Change in China from 2003 to 2019. *Int. J. Appl. Earth Obs. Geoinf.* **2021**, *104*, 102537. [CrossRef]
32. Estoque, R.C.; Murayama, Y.; Myint, S.W. Effects of Landscape Composition and Pattern on Land Surface Temperature: An Urban Heat Island Study in the Megacities of Southeast Asia. *Sci. Total Environ.* **2017**, *577*, 349–359. [CrossRef] [PubMed]
33. United States Geographic Survey (USGS). Available online: https://www.usgs.gov/ (accessed on 2 January 2023).
34. Earth Observation Group (EOG). Available online: https://eogdata.mines.edu/products/vnl/ (accessed on 20 February 2023).
35. Level 1 and Atmosphere Archive & Distribution System Distributed Active Archive Center (LAADS DAAC). Available online: https://ladsweb.modaps.eosdis.nasa.gov/search/order/1/MOD15A2H (accessed on 2 January 2023).
36. China Centre for Resource Satellite Data and Application (CASC). Available online: https://data.cresda.cn/ (accessed on 15 January 2023).
37. Barsi, J.; Schott, J.; Hook, S.; Raqueno, N.; Markham, B.; Radocinski, R. Landsat-8 Thermal Infrared Sensor (TIRS) Vicarious Radiometric Calibration. *Remote Sens.* **2014**, *6*, 11607–11626. [CrossRef]
38. Montanaro, M.; Lunsford, A.; Tesfaye, Z.; Wenny, B.; Reuter, D. Radiometric Calibration Methodology of the Landsat 8 Thermal Infrared Sensor. *Remote Sens.* **2014**, *6*, 8803–8821. [CrossRef]

39. Wang, F.; Qin, Z.; Song, C.; Tu, L.; Karnieli, A.; Zhao, S. An Improved Mono-Window Algorithm for Land Surface Temperature Retrieval from Landsat 8 Thermal Infrared Sensor Data. *Remote Sens.* **2015**, *7*, 4268–4289. [CrossRef]
40. Qin, Z.; Karnieli, A.; Berliner, P. A Mono-Window Algorithm for Retrieving Land Surface Temperature from Landsat TM Data and Its Application to the Israel-Egypt Border Region. *Int. J. Remote Sens.* **2001**, *22*, 3719–3746. [CrossRef]
41. Zhang, Y.; Li, L.; Chen, L.; Liao, Z.; Wang, Y.; Wang, B.; Yang, X. A Modified Multi-Source Parallel Model for Estimating Urban Surface Evapotranspiration Based on ASTER Thermal Infrared Data. *Remote Sens.* **2017**, *9*, 1029. [CrossRef]
42. Cecilia, A.; Casasanta, G.; Petenko, I.; Conidi, A.; Argentini, S. Measuring the Urban Heat Island of Rome through a Dense Weather Station Network and Remote Sensing Imperviousness Data. *Urban Clim.* **2023**, *47*, 101355. [CrossRef]
43. Khamchiangta, D.; Dhakal, S. Physical and Non-Physical Factors Driving Urban Heat Island: Case of Bangkok Metropolitan Administration, Thailand. *J. Environ. Manage.* **2019**, *248*, 109285. [CrossRef]
44. Hu, L.; Wilhelmi, O.V.; Uejio, C. Assessment of Heat Exposure in Cities: Combining the Dynamics of Temperature and Population. *Sci. Total Environ.* **2019**, *655*, 1–12. [CrossRef]
45. Vahmani, P.; Jones, A.D.; Patricola, C.M. Interacting Implications of Climate Change, Population Dynamics, and Urban Heat Mitigation for Future Exposure to Heat Extremes. *Environ. Res. Lett.* **2019**, *14*, 084051. [CrossRef]
46. Firozjaei, M.K.; Weng, Q.; Zhao, C.; Kiavarz, M.; Lu, L.; Alavipanah, S.K. Surface Anthropogenic Heat Islands in Six Megacities: An Assessment Based on a Triple-Source Surface Energy Balance Model. *Remote Sens. Environ.* **2020**, *242*, 111751. [CrossRef]
47. Gage, E.A.; Cooper, D.J. Relationships between Landscape Pattern Metrics, Vertical Structure and Surface Urban Heat Island Formation in a Colorado Suburb. *Urban Ecosyst.* **2017**, *20*, 1229–1238. [CrossRef]
48. Hou, H.; Estoque, R.C. Detecting Cooling Effect of Landscape from Composition and Configuration: An Urban Heat Island Study on Hangzhou. *Urban For. Urban Green.* **2020**, *53*, 126719. [CrossRef]
49. Gan, X.; Zhang, Y.; Wu, Z.; Wang, Y.; Han, H.; Yang, X. Spatial Characteristics of Urban Evapotranspiration Effects on the Thermal Environment. *J. Water Clim. Chang.* **2023**, *14*, 2103–2121. [CrossRef]
50. Liu, K.; Li, X.; Wang, S.; Gao, X. Assessing the Effects of Urban Green Landscape on Urban Thermal Environment Dynamic in a Semiarid City by Integrated Use of Airborne Data, Satellite Imagery and Land Surface Model. *Int. J. Appl. Earth Obs. Geoinf.* **2022**, *107*, 102674. [CrossRef]
51. Li, S.; Gao, Y.; Lyu, S.; Liu, Y.; Pan, Y. Response of Surface Air Temperature to the Change of Leaf Area Index in the Source Region of the Yellow River by the WRF Model. *Theor. Appl. Climatol.* **2019**, *138*, 1755–1765. [CrossRef]
52. Rakoto, P.Y.; Deilami, K.; Hurley, J.; Amati, M.; Sun, Q. (Chayn) Revisiting the Cooling Effects of Urban Greening: Planning Implications of Vegetation Types and Spatial Configuration. *Urban For. Urban Green.* **2021**, *64*, 127266. [CrossRef]
53. Zaitunah, A.; Samsuri, S.; Silitonga, A.F.; Syaufina, L. Urban Greening Effect on Land Surface Temperature. *Sensors* **2022**, *22*, 4168. [CrossRef]
54. Zhang, Y.; Wang, Y.; Ding, N.; Yang, X. Assessing the Contributions of Urban Green Space Indices and Spatial Structure in Mitigating Urban Thermal Environment. *Remote Sens.* **2023**, *15*, 2414. [CrossRef]
55. Yang, J.; He, Y.; Caspersen, J. Fully Constrained Linear Spectral Unmixing Based Global Shadow Compensation for High Resolution Satellite Imagery of Urban Areas. *Int. J. Appl. Earth Obs. Geoinf.* **2015**, *38*, 88–98. [CrossRef]
56. Li, L.; Canters, F.; Solana, C.; Ma, W.; Chen, L.; Kervyn, M. Discriminating Lava Flows of Different Age within Nyamuragira's Volcanic Field Using Spectral Mixture Analysis. *Int. J. Appl. Earth Obs. Geoinf.* **2015**, *40*, 1–10. [CrossRef]
57. Wang, C.; Chen, Z.; Yang, C.; Li, Q.; Wu, Q.; Wu, J.; Zhang, G.; Yu, B. Analyzing Parcel-Level Relationships between Luojia 1-01 Nighttime Light Intensity and Artificial Surface Features across Shanghai, China: A Comparison with NPP-VIIRS Data. *Int. J. Appl. Earth Obs. Geoinf.* **2020**, *85*, 101989. [CrossRef]
58. Dong, Y.; Varquez, A.C.G.; Kanda, M. Global Anthropogenic Heat Flux Database with High Spatial Resolution. *Atmos. Environ.* **2017**, *150*, 276–294. [CrossRef]
59. Chen, F.; Yang, X.; Wu, J. Simulation of the Urban Climate in a Chinese Megacity with Spatially Heterogeneous Anthropogenic Heat Data. *J. Geophys. Res.* **2016**, *121*, 5193–5212. [CrossRef]
60. Zhang, Q.; Schaaf, C.; Seto, K.C. The Vegetation Adjusted NTL Urban Index: A New Approach to Reduce Saturation and Increase Variation in Nighttime Luminosity. *Remote Sens. Environ.* **2013**, *129*, 32–41. [CrossRef]
61. Lu, D.; Tian, H.; Zhou, G.; Ge, H. Regional Mapping of Human Settlements in Southeastern China with Multisensor Remotely Sensed Data. *Remote Sens. Environ.* **2008**, *112*, 3668–3679. [CrossRef]
62. Chen, S.; Hu, D. Parameterizing Anthropogenic Heat Flux with an Energy-Consumption Inventory and Multi-Source Remote Sensing Data. *Remote Sens.* **2017**, *9*, 1165. [CrossRef]
63. Huang, W.; Cui, L.; Chen, M.; Zhang, D.; Yao, Y. Estimating Urban Functional Distributions with Semantics Preserved POI Embedding. *Int. J. Geogr. Inf. Sci.* **2022**, *36*, 1905–1930. [CrossRef]
64. He, B.; Hu, J.; Liu, K.; Xue, J.; Ning, L.; Fan, J. Exploring Park Visit Variability Using Cell Phone Data in Shenzhen, China. *Remote Sens.* **2022**, *14*, 499. [CrossRef]
65. Liang, S. Narrowband to Broadband Conversions of Land Surface Albedo I. *Remote Sens. Environ.* **2001**, *76*, 213–238. [CrossRef]
66. Chen, S.; Yang, Y.; Deng, F.; Zhang, Y.; Liu, D.; Liu, C.; Gao, Z. A High-Resolution Monitoring Approach of Canopy Urban Heat Island Using a Random Forest Model and Multi-Platform Observations. *Atmos. Meas. Tech.* **2022**, *15*, 735–756. [CrossRef]
67. Zhou, W.; Cao, F. Effects of Changing Spatial Extent on the Relationship between Urban Forest Patterns and Land Surface Temperature. *Ecol. Indic.* **2020**, *109*, 105778. [CrossRef]

68. Song, J.; Chen, W.; Zhang, J.; Huang, K.; Hou, B.; Prishchepov, A.V. Effects of Building Density on Land Surface Temperature in China: Spatial Patterns and Determinants. *Landsc. Urban Plan.* **2020**, *198*, 103794. [CrossRef]
69. Guo, L.; Liu, R.; Men, C.; Wang, Q.; Miao, Y.; Zhang, Y. Quantifying and Simulating Landscape Composition and Pattern Impacts on Land Surface Temperature: A Decadal Study of the Rapidly Urbanizing City of Beijing, China. *Sci. Total Environ.* **2019**, *654*, 430–440. [CrossRef] [PubMed]
70. Sun, X.; Tan, X.; Chen, K.; Song, S.; Zhu, X.; Hou, D. Quantifying Landscape-Metrics Impacts on Urban Green-Spaces and Water-Bodies Cooling Effect: The Study of Nanjing, China. *Urban For. Urban Green.* **2020**, *55*, 126838. [CrossRef]
71. Fei, Y.; Jiulin, S.; Hongliang, F.; Zuofang, Y.; Jiahua, Z.; Yunqiang, Z.; Kaishan, S.; Zongming, W.; Maogui, H. Comparison of Different Methods for Corn LAI Estimation over Northeastern China. *Int. J. Appl. Earth Obs. Geoinf.* **2012**, *18*, 462–471. [CrossRef]
72. Mu, Q.; Heinsch, F.A.; Zhao, M.; Running, S.W. Development of a Global Evapotranspiration Algorithm Based on MODIS and Global Meteorology Data. *Remote Sens. Environ.* **2007**, *111*, 519–536. [CrossRef]
73. Mu, Q.; Zhao, M.; Running, S.W. Improvements to a MODIS Global Terrestrial Evapotranspiration Algorithm. *Remote Sens. Environ.* **2011**, *115*, 1781–1800. [CrossRef]
74. Zhang, Y.; Li, L.; Qin, K.; Wang, Y.; Chen, L.; Yang, X. Remote Sensing Estimation of Urban Surface Evapotranspiration Based on a Modified Penman–Monteith Model. *J. Appl. Remote Sens.* **2018**, *12*, 1. [CrossRef]
75. Brunsdon, C.; Fotheringham, A.S.; Charlton, M.E. Geographically Weighted Regression: A Method for Exploring Spatial Nonstationarity. *Geogr. Anal.* **1996**, *28*, 281–298. [CrossRef]
76. Mohammadi, M.; Egli, M.; Kavian, A.; Lizaga, I. Static and Dynamic Source Identification of Trace Elements in River and Soil Environments under Anthropogenic Activities in the Haraz Plain, Northern Iran. *Sci. Total Environ.* **2023**, *892*, 164432. [CrossRef] [PubMed]
77. Zhang, Y.; Liu, Y.; Zhang, Y.; Liu, Y.; Zhang, G.; Chen, Y. On the Spatial Relationship between Ecosystem Services and Urbanization: A Case Study in Wuhan, China. *Sci. Total Environ.* **2018**, *637–638*, 780–790. [CrossRef] [PubMed]
78. Anselin, L. Local Indicators of Spatial Association—LISA. *Geogr. Anal.* **1995**, *27*, 93–115. [CrossRef]
79. Song, Y.; Wang, J.; Ge, Y.; Xu, C. An Optimal Parameters-Based Geographical Detector Model Enhances Geographic Characteristics of Explanatory Variables for Spatial Heterogeneity Analysis: Cases with Different Types of Spatial Data. *GIScience Remote Sens.* **2020**, *57*, 593–610. [CrossRef]
80. Schmid, H.P. Footprint Modeling for Vegetation Atmosphere Exchange Studies: A Review and Perspective. *Agric. For. Meteorol.* **2002**, *113*, 159–183. [CrossRef]
81. Stache, E.; Schilperoort, B.; Ottelé, M.; Jonkers, H.M. Comparative Analysis in Thermal Behaviour of Common Urban Building Materials and Vegetation and Consequences for Urban Heat Island Effect. *Build. Environ.* **2022**, *213*, 108489. [CrossRef]